Tectonic control on ^{10}Be-derived erosion rates in the Garhwal Himalaya, India

Dirk Scherler,[1,2] Bodo Bookhagen,[3] and Manfred R. Strecker[1]

Received 28 August 2013; revised 13 November 2013; accepted 26 November 2013; published 3 February 2014.

[1] Erosion in the Himalaya is responsible for one of the greatest mass redistributions on Earth and has fueled models of feedback loops between climate and tectonics. Although the general trends of erosion across the Himalaya are reasonably well known, the relative importance of factors controlling erosion is less well constrained. Here we present 25 ^{10}Be-derived catchment-averaged erosion rates from the Yamuna catchment in the Garhwal Himalaya, northern India. Tributary erosion rates range between ~0.1 and 0.5 mm yr^{-1} in the Lesser Himalaya and ~1 and 2 mm yr^{-1} in the High Himalaya, despite uniform hillslope angles. The erosion-rate data correlate with catchment-averaged values of 5 km radius relief, channel steepness indices, and specific stream power but to varying degrees of nonlinearity. Similar nonlinear relationships and coefficients of determination suggest that topographic steepness is the major control on the spatial variability of erosion and that twofold to threefold differences in annual runoff are of minor importance in this area. Instead, the spatial distribution of erosion in the study area is consistent with a tectonic model in which the rock uplift pattern is largely controlled by the shortening rate and the geometry of the Main Himalayan Thrust fault (MHT). Our data support a shallow dip of the MHT underneath the Lesser Himalaya, followed by a midcrustal ramp underneath the High Himalaya, as indicated by geophysical data. Finally, analysis of sample results from larger main stem rivers indicates significant variability of ^{10}Be-derived erosion rates, possibly related to nonproportional sediment supply from different tributaries and incomplete mixing in main stem channels.

Citation: Scherler, D., B. Bookhagen, and M. R. Strecker (2014), Tectonic control on ^{10}Be-derived erosion rates in the Garhwal Himalaya, India, *J. Geophys. Res. Earth Surf.*, *119*, 83–105, doi:10.1002/2013JF002955.

1. Introduction

[2] During the Indian summer monsoon season, torrential rivers flush large amounts of sediment from the rugged and high Himalayan ranges through deeply incised gorges into the Indo-Gangetic foreland and ultimately to the Bengal and Indus fans, the two largest submarine fans worldwide. These processes constitute one of the greatest mass transfers on the Earth's surface [*Milliman and Syvitski*, 1992], with potential impacts on the global carbon cycle and climate [e.g., *Raymo and Ruddiman*, 1992; *France-Lanord and Derry*, 1997; *Galy et al*., 2007]. Furthermore, the erosional flux in tectonically active mountain belts is an important component in the orogenic mass balance [e.g., *Koons*, 1990; *Willett*, 1999], and several studies argue for feedbacks between climate-driven erosion and tectonic deformation in the Himalaya [e.g., *Beaumont et al*., 2001; *Zeitler et al*., 2001; *Montgomery and Stolar*, 2006; *Thiede et al*., 2004; *Wobus et al*., 2005]. However, the validity of some of these models is debated [e.g., *Yin*, 2006; *Herman et al*., 2010; *Webb et al*., 2011a, 2011b]. A better understanding of the processes and rates of erosion in the Himalaya and their relation to different forcing factors is therefore an important issue for assessing such linkages. In addition, if topography is approximately in steady state [cf., *Willett and Brandon*, 2002], landscape-scale erosion rates should equal tectonic rock uplift rates and therefore provide unique insights into subsurface structures and active tectonics [e.g., *Lavé and Avouac*, 2001; *Kirby and Whipple*, 2012].

[3] *Seeber and Gornitz* [1983] were among the first to infer spatial patterns of fluvial incision across the Himalaya, based on channel gradients of transverse rivers along the Himalayan arc. Systematic across-strike changes in river steepness between the rugged High Himalaya (HH) and the Lesser Himalaya (LH) led these authors to deduce variations in fluvial incision rates, which they inferred to be in balance with rock uplift rates and helped them to distinguish between different tectonic models. In two more recent studies, *Lavé and Avouac* [2000, 2001] took a similar but more mechanistic approach to derive river incision rates across the Himalaya of Central Nepal. Based on Holocene strath terraces, they found

Additional supporting information may be found in the online version of this article.

[1]Institute of Earth and Environmental Science, Universität Potsdam, Potsdam, Germany.
[2]Geological and Planetary Sciences, California Institute of Technology, Pasadena, California, USA.
[3]Department of Geography, University of California, Santa Barbara, California, USA.

Corresponding author: D. Scherler, Geological and Planetary Sciences, California Institute of Technology, Pasadena, CA 91125, USA. (scherler@caltech.edu)

2169-9003/14/10.1002/2013JF002955

that actively growing anticlines in the weakly lithified Sub-Himalayan lithologies (i.e., the Himalayan Molasse) are incising with ~10–15 mm yr^{-1}, corresponding to a shortening rate across the Main Frontal Thrust of ~20 mm yr^{-1} [*Lavé and Avouac*, 2000]. Terraces and channel geometries at the transition to the LH to the north indicate that incision rates drop by about an order of magnitude to ~0.5–2 mm yr^{-1}. Farther northward, at the transition from the LH to the HH, channel geometries indicate an increase of incision rates to about ~4–8 mm yr^{-1} [*Lavé and Avouac*, 2001]. The inferred rates in the LH and HH are approximately similar to suspended sediment-load records [*Lavé and Avouac*, 2001], while the spatial pattern is also reflected in compositional variations of modern river sediments [*Garzanti et al*., 2007]. The shear stress approach of *Lavé and Avouac* [2001], however, heavily depends on calibrating the channel geometries to independently constrained incision rates, which were rather limited in the LH and HH when the study was carried out. Furthermore, most transverse Himalayan rivers have repeatedly incised and aggraded at some point during their late Pleistocene and Holocene history [e.g., *Lavé and Avouac*, 2001; *Pratt et al*., 2002; *Bookhagen et al*., 2005; *Srivastava et al*., 2008] and some may not have reached their former bedrock level again [e.g., *Lavé and Avouac*, 2001], thus complicating the along-stream calibration of channel geometries.

[4] Subsequent studies that used different approaches generally corroborated the spatial pattern of erosion but often obtained somewhat lower rates in the HH. The most recent erosion-rate estimate that is based on gauged suspended sediment fluxes from the Central Himalaya yields ~0.2–2 mm yr^{-1} in the LH and ~0.5–2.8 mm yr^{-1} in the HH [*Andermann et al*., 2012]. Similar rates have been obtained from smaller catchments in the Nepalese Marsyandi Valley [*Gabet et al*., 2008] or the Indian Sutlej Valley, farther west [*Wulf et al*., 2010, 2012]. However, these rates are based on suspended loads only, covering a maximum of a few decades of data, and the additional contribution through bed load and the dissolved fraction could be substantial in steep areas or carbonate-rich lithologies, respectively [*Pratt-Sitaula et al*., 2007; *France-Lanord et al*., 2003; *Tripathy and Singh*, 2010; *Wulf et al*., 2010]. In addition, suspended load and discharge-based fluxes can have large uncertainties and may suffer from timescale issues when sediment transport is strongly varying with time [e.g., *Kirchner et al*., 2001; *Wulf et al*., 2010].

[5] Several studies have used terrestrial cosmogenic nuclides to determine catchment-averaged erosion rates in different parts of the Himalaya. Cosmogenic nuclides are rare isotopes that are produced by cosmic rays in the upper few meters of the Earth's surface. Their abundance in fluvial sediments provides a catchment-averaged erosion-rate estimate over ~10^2–10^5 year timescales, depending on the erosion-rate magnitude [*von Blanckenburg*, 2005]. In fluvial dominated catchments, these studies have yielded erosion rates of ~0.1–1 mm yr^{-1} in the LH that increase to ~1–3 mm yr^{-1} in the HH [*Vance et al*., 2003; *Wobus et al*., 2005; *Godard et al*., 2012]. Similar erosion rates (~0.5–2.4 mm yr^{-1}) were derived for entire watersheds of several major Himalayan rivers [*Lupker et al*., 2012], but these rates do not discriminate between LH and HH sources. Yet other studies have determined long-term exhumation rates from mineral-cooling ages (see overview in *Thiede and Ehlers* [2013]) and yielded erosion-rate estimates that are on average in between estimates based on recent sediment loads and those determined by *Lavé and Avouac* [2001]. The integration timescale of such methods, however, is usually on the order of 10^6 years and they are therefore more suitable for detecting long-term tectonic activity, whereas potential changes in exhumation rate that may have occurred, e.g., during the Quaternary climatic fluctuations, may be missed out.

[6] Despite some differences in erosion magnitudes, the general erosion pattern deduced by *Lavé and Avouac* [2000, 2001] and subsequent workers can be well matched with a rock uplift pattern that would be expected for a ramp in the crustal-scale décollement which is an integral part of the Main Himalayan Thrust fault [*Cattin and Avouac*, 2000; *Godard et al*., 2004], a structural scenario which is also consistent with several geophysical observations [e.g., *Avouac*, 2003; *Caldwell et al*., 2013]. Although most authors acknowledge the overarching contribution of monsoonal rainfall to discharge and erosion in this region [e.g., *Masek et al*., 1994; *Galy and France-Lanord*, 2001; *Clift et al*., 2008; *Rahaman et al*., 2009], the degree of coupling between rainfall and erosion is not straightforward [e.g., *Burbank et al*., 2003]. Is the spatial distribution of erosion in the Himalaya merely a function of largely structurally controlled rock uplift or do rainfall magnitudes influence erosion rates —and if so, to which degree? The coincidence of a steep increase in erosion rates at the transition from the LH to the HH with an abrupt rise in focused monsoonal rainfall [*Burbank et al*., 2003] has led to ample speculations about climate-driven feedbacks between erosion and tectonics [e.g., *Beaumont et al*., 2001; *Hodges et al*., 2004; *Thiede et al*., 2004; *Wobus et al*., 2005]. More recently, satellite-derived observations have shown that orographic rainfall in the Himalaya consists of one or two narrow orographic rainfall bands, located at distinct and constant elevation intervals [*Bookhagen and Burbank*, 2006]. Surprisingly, the more consistent and pronounced outer rainfall band along the southern Himalayan flank is located at the first topographic rise (~900 ± 400 m elevation) over the more slowly eroding and vegetated LH.

[7] In the following, we present a systematic study of catchment-averaged erosion rates based on ^{10}Be abundances in river sediments from small to medium-sized catchments (9–548 km^2) across the Yamuna catchment, in the Garhwal Himalaya, India, which hosts the westernmost Himalayan headwaters of the Ganges River (Figure 1). We used these data to analyze the magnitudes and spatial variations of erosion rates with respect to different hydromorphometric parameters, such as local relief, channel steepness, and specific stream power. This area is well suited for such analysis, because it (1) is dominated by quartz-rich lithologies, (2) is only marginally influenced by glaciation, (3) features two orographic rainfall bands, and (4) presumably spans a relatively wide range of uplift rates. However, estimating erosion rates from cosmogenic nuclides follows a set of assumptions, which are potentially violated in rapidly eroding landscapes due to episodic mass wasting and sediment transport processes [e.g., *Niemi et al*., 2005; *Binnie et al*., 2006]. Such potential problems were difficult to evaluate in previous studies from the Himalaya where the sampling strategy did not allow a more systematic analysis. To assess these issues, we sampled tributaries as well as main stem rivers to analyze the downstream evolution of ^{10}Be concentrations. Specifically, we compared ^{10}Be-derived main stem erosion rates with those predicted from calibrated

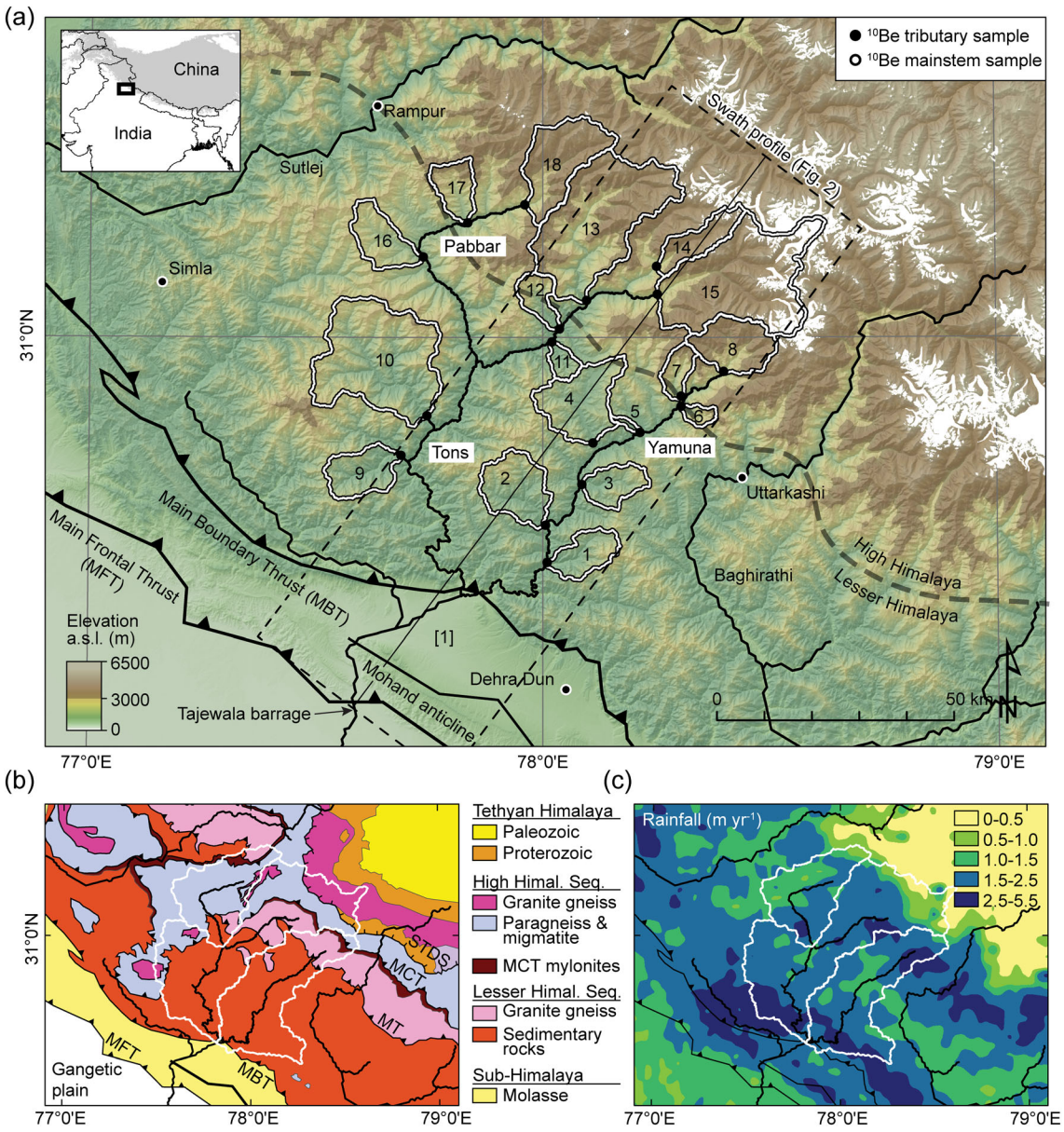

Figure 1. Overview of the study area in the Garhwal Himalaya, NW India. (a) Elevation map draped over hillshade map showing Yamuna catchment, sample locations, and sampled tributary catchments. Numbers and letter-number combinations refer to sample IDs given in Table 1 and Table 2. Black lines in tributary catchment #15 give mapped moraines after *Scherler et al*. [2010]. (b) Bedrock geology after *Vannay et al*. [2004]. (c) Annual rainfall after *Bookhagen and Burbank* [2010].

functional relationships of the tributary data with several hydromorphometric parameters.

2. Study Area

2.1. The Yamuna Catchment

[8] In our study we focused on the Yamuna River and its two major Himalayan tributaries, the Pabbar and Tons Rivers (Figure 1). The Yamuna Valley has a relatively small but very steep high-alpine area, with almost no current ice cover and, apart from one tributary, no indication of significant ice cover during recent glacial periods. Northwest of the Yamuna lies the Tons Valley, which has a much larger high-alpine area with ~125 km^2 present-day ice cover and evidence for glaciers extending down to an elevation of approximately 2500 m above present sea level at ~16 kyr [*Scherler et al*., 2010]. The confluence of the Yamuna and Tons Rivers is located right next to where they enter the Dehra Dun Valley, an up to ~15 km wide piggyback basin that borders the LH to the south [*Singh et al*., 2001]. The Pabbar River is a tributary to the Tons River and its valley hosts almost no glaciers at present (<1 km^2), but moraines and valley morphologies in its upper reaches suggest a somewhat greater ice coverage in the past. A 50 km wide swath profile across our study area and perpendicular to the strike of the mountain range shows the gradual increase of mean surface elevations. Starting at ~300–800 m in the Dehra Dun Valley, elevations rise across the LH to ~2000 m at a

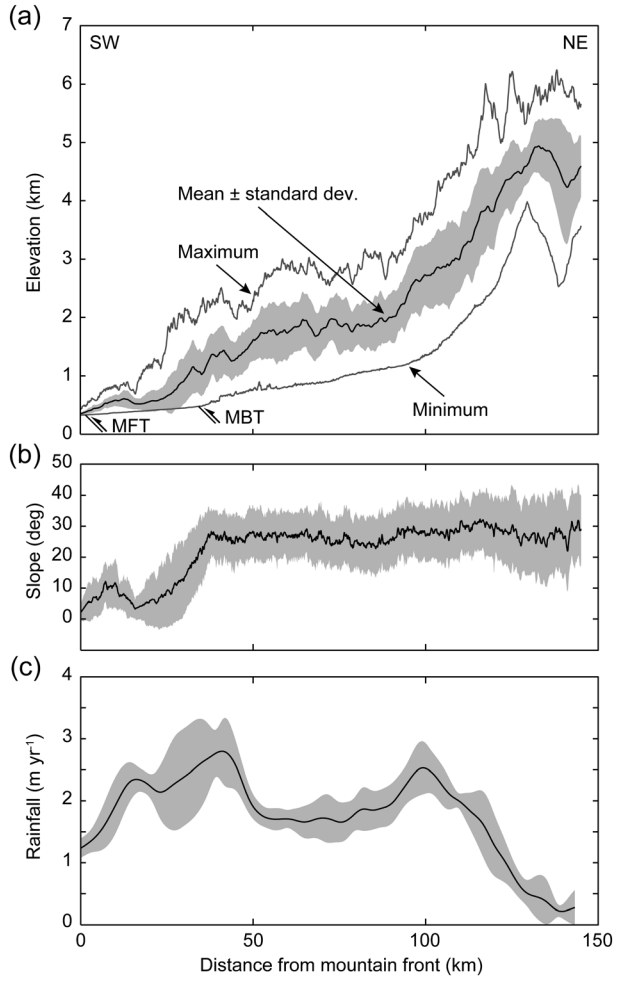

Figure 2. Swath profile (50 km wide), showing the distribution of (a) surface elevation, (b) surface slope, and (c) annual rainfall, from SW to NE across the western Garhwal Himalaya. See Figure 1 for footprint. MFT = Main Frontal Thrust, MBT = Main Boundary Thrust.

distance of ~90 km and then in the HH more steeply to ~5000 m at the crest of the range and at a distance of ~130 km from the mountain front at the Main Frontal Thrust (MFT; Figure 2a). In contrast to these large differences in relief, mean slope angles rise to values of ~25° in the LH, upstream of the Dehra Dun Valley, and remain relatively constant throughout the entire catchment (Figure 2b).

2.2. Geological and Structural Setting

[9] The bedrock geology in the study area displays the characteristic inverted metamorphic sequence that is found throughout much of the Himalaya (Figure 1b) [*Gansser*, 1964; *Vannay et al*., 2004; *Yin*, 2006]. Near the Tajewala barrage (Figure 1a), the Yamuna River crosses the active Main Frontal Thrust (MFT), along which the partly faulted and folded Sub-Himalayan Molasse units (Siwaliks) are thrusted onto the undeformed Gangetic foreland, forming the first topographic rise with the Mohand anticline [*Srivastava and Mitra*, 1994; *Powers et al*., 1998]. At the transition from the Dehra Dun Valley to the LH, the Main Boundary Thrust (MBT) separates the Sub-Himalaya from the low-grade metamorphic metasedimentary rocks of the Lesser Himalayan Sequence (LHS) that dominate the lower part of the Yamuna catchment. To the north and structurally higher, the low-grade metamorphic LHS rocks are separated by the Munsiari Thrust (MT) from higher-metamorphic granitic gneisses of the LHS. The LHS crystalline rocks are themselves separated by mylonites of the Main Central Thrust (MCT, locally also known as the Vaikrita Thrust) from high-grade metamorphic gneisses, migmatites, and granites of the High Himalayan Sequence (HHS). Because of its greater northward extent, the high-altitude areas of the Tons Valley are dominated by HHS rocks. Note that we use the terms LH and HH to refer to the physiographic regions, approximately concordant with areas where peak elevations are below and above ~3000 m, respectively, whereas LHS and HHS refer to the tectonostratigraphic rock units.

[10] Recent teleseismic receiver-function studies in Garhwal indicate that the basal décollement of the Main Himalayan Thrust fault (MHT) is at a depth of ~10 km and dipping north at only ~2° beneath the northern LH before it connects to a ~16° dipping midcrustal ramp [*Caldwell et al*., 2013], approximately beneath the transition to the HH. Farther southwest, in the Dehra Dun Valley, seismic reflection profiles indicate the MHT at a depth of ~4–5 km, and dipping with ~6° to the northeast, potentially steepening underneath the MBT [*Powers et al*., 1998]. The exposed rocks in the Pabbar Valley belong almost entirely to the HHS, which extends in the northwestern part of the study area much farther southwest toward the mountain front, above an almost flat-lying segment of the MCT (Figure 1b). Note that there exist different interpretations as to the tectonostratigraphic association of these rocks in the Pabbar Valley [e.g., *Webb et al*., 2011a, 2011b]. *Thiede et al*. [2009] obtained apatite fission track data that mostly stem from the HHS in the northern and northwestern part of the Yamuna catchment and which indicate average exhumation rates of ~1–2 mm yr^{-1} over the last ~2–10 Myr.

2.3. Climate and Hydrology

[11] The study area is influenced by two atmospheric circulation systems, the southwest Indian monsoon during summer and the Westerlies during winter [*Scherler et al*., 2010; *Wulf et al*., 2010]. The majority of precipitation occurs from June to September, when humid air masses of the Indian monsoon impinge on the mountain front [*Bookhagen and Burbank*, 2010]. The across-strike variations in surface elevation coincide with a pronounced two-banded rainfall pattern (Figure 2c). The outer band of high rainfall (>2.5 m yr^{-1}) is located over the LH, just north of the MBT, whereas the inner band is located near the MT at the physiographic transition of the LH to the HH and is less well expressed in the northwestern part of the Yamuna catchment. Most other areas receive rainfall of 1.0–2.5 m yr^{-1} (Figure 1c), and the generally humid climate sustains a dense forest cover where human influence is low and agriculture where hillslope angles are low, such as on fill terraces. At elevations >3000 m, annual rainfall steeply decreases northward, whereas snowfall increases [*Wulf et al*., 2010], and vegetation cover gets gradually replaced by bare rock. According to *Rao* [*Rao*, 1975; cited in *Jha et al*., 1988 and *Dalai et al*., 2002] the total annual discharge of the Yamuna River at the Tajewala barrage is ~10.5 km^3 yr^{-1}, equaling ~1.1 m yr^{-1} runoff, with ~78% occurring during the monsoon season.

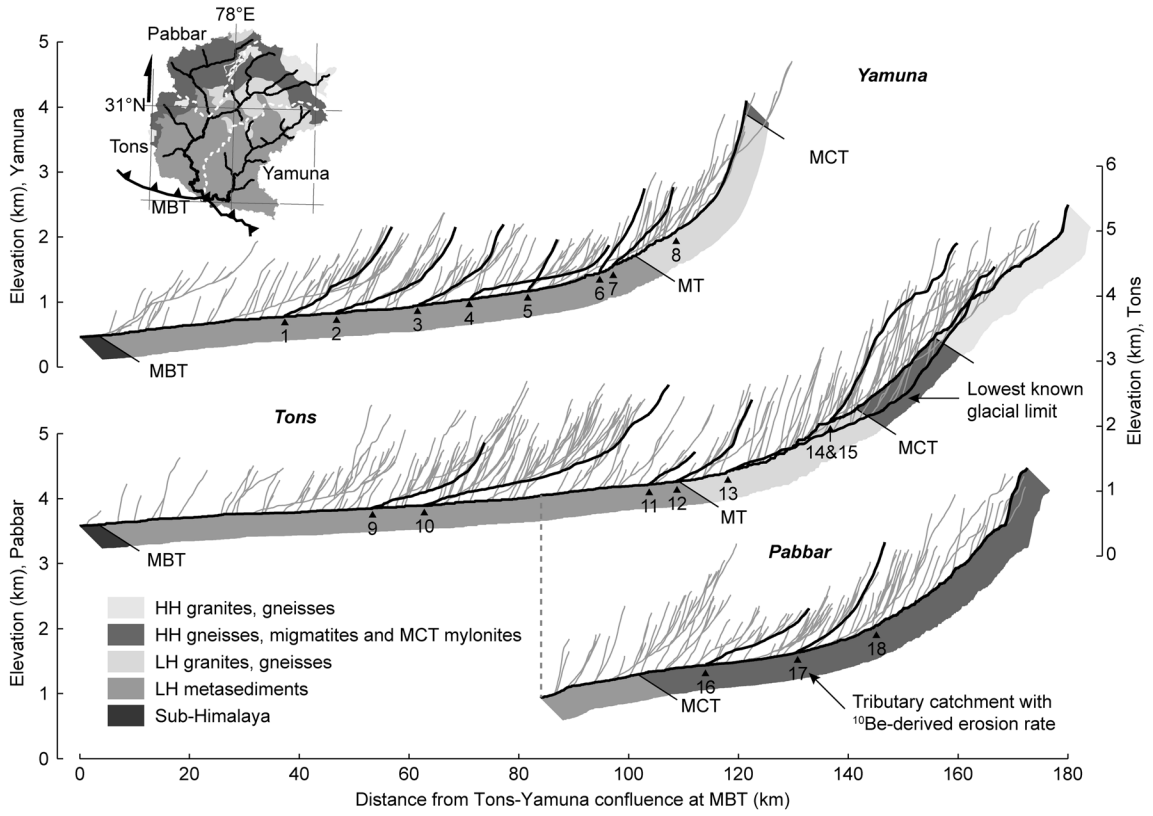

Figure 3. Longitudinal river profiles of main drainages (from top to bottom Yamuna, Tons, Pabbar) in the Yamuna catchment. Tributaries with upstream areas >1 km^2 are shown by gray thin lines and sampled tributaries by black bold lines. Triangles with numbers denote outlets of sampled tributaries (see Figure 1). Bedrock geology is shown in inset figure and depicted by gray-shaded colors below profiles. MBT = Main Boundary Thrust, MT = Munsiari Thrust, MCT = Main Central Thrust.

2.4. Geomorphic Setting

[12] In this study, we focused our analysis on 18 catchments that are tributaries to the three main stem rivers and have upstream areas between 9 and 548 km^2. Their river channels expose either bedrock or a thin alluvial cover, and only few of them show signs of more extended (tributary #4) or localized valley fills (tributary #1). Most of the tributary channels in the Yamuna, Pabbar, and lower Tons appear to be characterized by concave-up graded profiles that are typical for fluvial channels [*Hack*, 1957]. However, there are also a few tributaries that contain pronounced knickpoints or zones (Figure 3). Some knickpoints seen in tributaries of the lowermost Yamuna Valley appear to separate a high-relief lower from a low-relief upper portion of the catchment, pointing at transient channel adjustment. In tributary #1 this adjustment appears spatially more restricted and coincident with an epigenetic gorge [e.g., *Ouimet et al*., 2008] next to a localized valley fill. The reaches of tributary channels in the upper Tons that were previously glaciated [cf., *Scherler et al*., 2010] have more gentle gradients than what would be expected for a graded profile and thus document the glacial overprint [e.g., *Brocklehurst and Whipple*, 2004]. One phenomenon not readily explained by transient adjustment or glacial overprint is the extremely gentle channel gradient of tributary #4, which stands out among all other tributaries. We will analyze this tributary in more detail in the discussion section.

[13] Based on modern river sediments, collected approximately 10 km downstream of the Tons-Yamuna confluence, *Lupker et al*. [2012] obtained a ^{10}Be-derived erosion rate of 0.7 ± 0.3 mm yr^{-1} for the entire Yamuna catchment. This value is comparable to a catchment-averaged erosion rate of ~1.0 mm yr^{-1} based on suspended and dissolved loads collected at the Tajewala barrage [*Jha et al*., 1988]. The latter value, however, is based on only three samples, which were collected during 1983. Dissolved constituents in Yamuna waters suggest an average chemical erosion rate of ~0.01 mm yr^{-1} from silicates and ~0.04 mm yr^{-1} from carbonates [*Dalai et al*., 2002]. Up to ~100 m thick fluvial fill terraces are found in several places along the main stem rivers and document a period of catchment-wide aggradation, when sediment supply was greater than the transport capacity of the rivers. Similar deposits exist in the Sutlej Valley to the west [*Bookhagen et al*., 2006] and the Bhagirathi and Alaknanda Valley to the east [*Srivastava et al*., 2008]. The terrace surfaces are generally used for agriculture, and isolated patches can sometimes be traced several kilometers into tributaries, where they appear less well preserved or developed. We will examine these fill terraces more closely in a separate study but have to consider their potential influence on our samples in this study.

3. Data and Methods

3.1. Cosmogenic Nuclide-Derived Erosion Rates

3.1.1. Sampling Strategy and Analytical Procedures

[14] For estimating catchment-averaged erosion rates with in situ produced ^{10}Be [e.g., *Brown et al*., 1995; *Bierman and Stieg*, 1996; *Granger et al*., 1996; *von Blanckenburg*, 2005], we

Table 1. Catchment Characteristics

		Elevation (m)	Rainfall[b] (mm yr^{-1})		Discharge[c](m^3 yr^{-1})		Runoff (m yr^{-1})		Outcropping Rock Units[d] (%)					
ID[a]	Area (km^2)	Mean	Mean	S.D.	Q = R	Q = R-ET + M	Q = R	Q = R-ET + M	LH-SR	LH-GG	MCT	HH-PM	HH-GG	TH
Yamuna Tributaries														
1	100	1808	1893	251	6.0	5.8	1.9	1.8	100	0	0	0	0	0
2	168	1840	1649	171	8.8	8.8	1.6	1.6	100	0	0	0	0	0
3	89	1881	1517	95	4.3	3.3	1.5	1.2	100	0	0	0	0	0
4	210	1893	1790	299	11.9	11.3	1.8	1.7	79	21	0	0	0	0
5	9	1832	1465	129	0.4	0.4	1.5	1.3	100	0	0	0	0	0
6	25	2539	2660	121	2.1	2.3	2.7	2.9	62	38	0	0	0	0
7	55	2738	2179	214	3.8	3.6	2.2	2.0	50	50	0	0	0	0
8	160	3558	2098	292	10.6	11.4	2.1	2.3	0	67	23	10	0	0
Tons Tributaries														
9	128	1704	2994	435	12.2	11.5	3.0	2.8	99	0	0	1	0	0
10	514	2126	1835	273	29.9	27.1	1.8	1.7	42	0	0	52	6	0
11	36	1724	2131	168	2.4	2.1	2.1	1.8	99	1	0	0	0	0
12	66	2269	2116	116	4.4	4.0	2.1	1.9	5	50	0	45	0	0
13	536	3296	1737	383	29.5	29.9	1.7	1.8	0	15	3	68	14	0
14	103	4142	1260	691	4.1	5.9	1.3	1.8	0	1	4	49	46	0
15	548	4282	1163	627	20.2	30.6	1.2	1.8	0	14	5	38	35	8
Pabbar Tributaries														
16	123	2290	1247	135	4.9	4.6	1.2	1.2	0	0	0	100	0	0
17	88	2702	1241	156	3.5	3.5	1.2	1.3	0	0	0	100	0	0
18	231	3739	1405	403	10.3	11.2	1.4	1.5	0	27	9	55	10	0
Main Stems														
Y1	647	2976	2234	459	45.8	48.3	2.2	2.4	39	45	8	8	0	0
Y2	1179	2474	1962	492	73.3	73.2	2.0	2.0	63	28	4	5	0	0
P1	516	3315	1447	308	23.6	24.2	1.4	1.5	3	13	11	66	7	0
P2	1440	2679	1578	405	72.0	65.6	1.6	1.4	11	10	4	72	3	0
T1	3477	3015	1624	544	179.0	183.0	1.6	1.7	13	19	3	51	12	1
T2	4670	2750	1721	550	254.8	253.5	1.7	1.7	28	14	2	44	10	1
Y3	7571	2426	1880	606	451.3	447.5	1.9	1.9	49	13	2	28	6	1

[a]ID = Tributary number shown in Figure 1; main stem sample abbreviations: Y = Yamuna, T = Tons, P = Pabbar.
[b]Annual rainfall determined from 10 years of Tropical Rainfall Measuring Mission (TRMM) data. S.D. = Standard deviation.
[c]Discharge (Q) based on TRMM rainfall (R), modeled evapotranspiration (ET), and snowmelt (M); see *Bookhagen and Burbank* [2010] for details.
[d]Abbreviations of rock units: LH-SR = Lesser Himalaya metasedimentary rocks, LH-GG = Lesser Himalaya granites and gneisses, MCT = Main Central Thrust mylonites, HH-PM = Higher Himalaya paragneisses and migmatites, HH-GG = Higher Himalaya granites and gneisses, TH = Tethyan Himalaya sedimentary rocks.

collected river sand samples from active channels throughout the study area. We generally avoided localities where nearby landslides or construction work could potentially dominate the sediment source of the sample. We collected samples from 17 tributaries with upstream areas of 9 to 548 km^2, most of which drain catchments of relatively uniform lithology and climate (Figure 3 and Table 1). Among the tributary samples, we have one replicate sample pair (DS-AR3 and DS7-051), taken in consecutive years (Table 2). We further collected two samples each from the active channels of the three main stem rivers and included a sample (YAM-Q3) collected by *Lupker et al.* [2012] in the Dehra Dun Valley in our calculation of erosion rates (Figure 1a).

[15] Physical and chemical separation of the 125–500 μm sized quartz fraction of all samples was done at the University of Potsdam, following standard procedures [e.g., *Kohl and Nishiizumi*, 1992], and included magnetic and heavy-liquid separation, carbonate dissolution with heated hydrochloric acid (19%), and repeated leaching with a heated 1:1 hydrofluoric (2%) and nitric (2%) acid solution in ultrasonic baths. ^{10}Be extraction by ion exchange chromatography and target preparation was done at the University of California Santa Barbara, following established protocols [e.g., *von Blanckenburg et al.*, 2004; *Bookhagen and Strecker*, 2012]. Accelerator mass spectrometry measurements were carried out at the Center for Accelerator Mass Spectrometry, Lawrence Livermore National Laboratories, USA. All ^{10}Be/^{9}Be ratios were normalized to the standard 07KNSTD3110, with a nominal ^{10}Be/^{9}Be ratio of 2.85×10^{-12} [*Nishiizumi et al.*, 2007].

3.1.2. Calculation of Erosion Rates

[16] We converted the ^{10}Be concentrations of our samples into catchment-averaged erosion rates, following the theoretical framework of previous studies [e.g., *Brown et al.*, 1995; *Bierman and Stieg*, 1996; *Granger et al.*, 1996] and using the numerical functions of the CRONUS-Earth online calculator version 2.2 [http://hess.ess.washington.edu/math/al_be_v22/functionlist.html; *Balco et al.*, 2008]. Erosion rates were calculated in an iterative scheme based on a catchment-averaged production rate vector, the same way it is done in the CRONUS-Earth online calculator for point-based erosion rate estimates (see supporting information for a short summary, and *Balco et al.* [2008], for a more detailed description). Reported erosion rates are based on the revised ^{10}Be half-life of 1.387±0.016 Myr [*Chmeleff et al.*, 2010; *Korschinek et al.*, 2010] and a time-dependent form of the Lal/Stone scaling procedure [*Lal*, 1991; *Stone*, 2000], which is taking muogenic production and nondipole geomagnetic field effects into account (denoted "Lm" in *Balco et al.* [2008]). Results for other scaling models are given in the supporting information Table S1.

[17] The catchment-averaged time-dependent production rate vectors were computed as the arithmetic mean of all production-rate vectors within a given catchment, which

Table 2. ^{10}Be Analytical and Derived Erosion Rate Data

ID[a]	Sample	Latitude (°N)	Longitude (°E)	^{10}Be Concentration[b] (1e3 atoms g^{-1})	Shielding Factors[c]				Surface-Production Rate[d] (atoms g^{-1} yr^{-1})		Erosion Rate Without Snow Shielding[e] (mm yr^{-1})	Erosion Rate With Snow Shielding[e] (mm yr^{-1})
					Topography	Ice	Snow	Total	Muogenic	Spallogenic		
					Yamuna Tributaries							
1	DS7-048	30.573382	78.007267	18.70 ± 0.67	0.97	1.00	1.00	0.96	0.33	14.18	0.55 ± 0.04	0.55 ± 0.04
2	DS7-049	30.641571	78.006942	66.37 ± 1.66	0.97	1.00	1.00	0.96	0.33	14.54	0.16 ± 0.01	0.16 ± 0.01
3	DS6-AR3	30.722153	78.088039	74.70 ± 1.58	0.97	1.00	1.00	0.97	0.33	14.87	0.15 ± 0.01	0.15 ± 0.01
3	DS7-051	30.722153	78.087148	49.01 ± 1.25	0.97	1.00	1.00	0.97	0.33	14.87	0.22 ± 0.02	0.22 ± 0.02
4	DS7-061	30.799778	78.112032	85.24 ± 2.13	0.97	1.00	1.00	0.97	0.34	14.95	0.13 ± 0.01	0.13 ± 0.01
5	DS7-045	30.820332	78.207377	139.03 ± 3.46	0.97	1.00	1.00	0.97	0.33	14.35	0.08 ± 0.01	0.08 ± 0.01
6	DS7-044	30.872857	78.303697	47.41 ± 1.20	0.95	1.00	0.99	0.94	0.41	21.98	0.32 ± 0.02	0.32 ± 0.02
7	DS6-006	30.888233	78.305386	13.69 ± 0.32	0.94	1.00	0.96	0.90	0.43	24.01	1.22 ± 0.09	1.17 ± 0.09
8	DS6-008	30.933358	78.400923	4.76 ± 0.19	0.94	1.00	0.87	0.82	0.55	33.84	5.37 ± 0.46	4.59 ± 0.39
					Tons Tributaries							
9	DS7-077	30.776664	77.686997	24.59 ± 0.58	0.96	1.00	1.00	0.96	0.32	13.15	0.39 ± 0.03	0.39 ± 0.03
10	DS7-072	30.849383	77.744701	42.60 ± 0.92	0.96	1.00	1.00	0.96	0.36	17.69	0.29 ± 0.02	0.29 ± 0.02
11	DS7-062	30.990885	78.019605	66.33 ± 1.98	0.97	1.00	1.00	0.96	0.32	13.17	0.15 ± 0.01	0.15 ± 0.01
12	DS7-066	31.019621	78.035421	24.56 ± 0.70	0.94	1.00	0.99	0.93	0.38	18.97	0.54 ± 0.04	0.53 ± 0.04
13	DS6-081	31.068955	78.098216	11.40 ± 0.35	0.95	1.00	0.91	0.86	0.51	31.81	2.05 ± 0.17	1.81 ± 0.14
14	DS6-080A	31.137256	78.252748	17.21 ± 0.43	0.93	0.93	0.80	0.70	0.64	37.94	1.78 ± 0.14	1.41 ± 0.11
15	DS6-023C	31.082113	78.253563	11.31 ± 0.34	0.94	0.81	0.79	0.63	0.66	34.12	2.44 ± 0.20	1.97 ± 0.16
					Pabbar Tributaries							
16	DS7-088	31.153641	77.736255	44.05 ± 1.13	0.98	1.00	1.00	0.97	0.38	19.55	0.31 ± 0.02	0.31 ± 0.02
17	DS7-086	31.2195	77.829305	58.75 ± 1.44	0.96	1.00	0.98	0.95	0.43	25.00	0.29 ± 0.02	0.29 ± 0.02
18	DS6-088	31.252447	77.960439	26.83 ± 0.75	0.95	1.00	0.87	0.82	0.57	37.81	1.06 ± 0.09	0.90 ± 0.07
					Main Stems							
Y1	DS7-055	30.820233	78.229021	15.56 ± 0.35	0.95	0.99	0.93	0.88	0.47	26.80	1.26 ± 0.10	1.14 ± 0.09
Y2	DS6-018	30.72526	78.07956	47.72 ± 1.34	0.96	0.99	0.96	0.92	0.41	21.34	0.33 ± 0.03	0.31 ± 0.02
P1	DS6-094	31.226277	77.852679	60.63 ± 1.46	0.96	1.00	0.92	0.88	0.51	32.70	0.39 ± 0.03	0.35 ± 0.03
P2	DS6-085	30.954612	77.853222	33.52 ± 0.86	0.96	1.00	0.97	0.93	0.43	24.61	0.52 ± 0.04	0.49 ± 0.04
T1	DS7-071	30.92177	77.83921	14.46 ± 0.43	0.95	0.96	0.92	0.86	0.48	26.74	1.37 ± 0.11	1.22 ± 0.10
T2	DS7-076	30.760827	77.704418	14.18 ± 0.54	0.96	0.97	0.94	0.88	0.45	24.01	1.25 ± 0.10	1.13 ± 0.09
Y3	YAM-Q3[f]	30.454068	77.702043	21.40 ± 2.10	0.96	0.98	0.96	0.91	0.41	20.83	0.72 ± 0.09	0.66 ± 0.08

[a]ID = Tributary number shown in Figure 1; main stem sample abbreviations: Y = Yamuna, T = Tons, P = Pabbar.

[b]In situ produced cosmogenic nuclide concentrations based on sample mass and ^{10}Be/^{9}Be ratios, normalized to standard 07KNSTD3110 with a nominal ^{10}Be/^{9}Be value of 2.85e-12 [*Nishiizumi et al.*, 2007]. The subtracted average laboratory process blank ^{10}Be/^{9}Be ratio is 4.0×10^{-15}.

[c]Snow cover shielding based on modeled snow thicknesses (see text for details), assuming a maximum snow depth of 5 m and snow density of 0.25 g cm^{-3}.

[d]Production rate according to time-dependent Lal/Stone scaling, see text and *Balco et al.* [2008] for details.

[e]Erosion rates (with units L/T) based on an assumed bedrock density of 2.7 g cm^{-3}.

[f]^{10}Be sample results from *Lupker et al.* [2012]. Erosion rates were recalculated using production rates and shielding factors determined for the present study.

were calculated on a pixel basis using the 90 m resolution digital elevation model (DEM). Some of the LHS metasedimentary rocks contain carbonate-rich rocks which would contribute little or no quartz to our samples. As rock types in the LHS change frequently in the stratigraphic sequence, it is difficult to properly account for this effect. According to the mapping of *Webb et al*. [2011a, 2011b], the up to ~2000 m thick upper-LHS Deoban Formation consists predominantly of dolomites and limestones, with minor shales and sandstones, and makes up ~80% of the areas of the sampled tributaries #3 and #5 and <20% of the areas in tributaries #2, #4, #9, and #10. Exclusion of these areas when calculating production rates changes the erosion rates by ~72% and 80% and ~31%, 19%, 2%, and 8%, respectively. However, it is surprising that all of these samples yielded a significant amount of quartz and only the samples from tributaries #2 and #10 suffered appreciable (>40%) mass losses during hydrochloric leaching, while the other four samples lost <10% mass only (Table S2). Geochemical analysis from bed load in the adjacent Bhagirathi and Alaknanda catchments indicates a mean modal quartz (carbonate) content of 34% (33%) in the Deoban Formation [*Vance et al*., 2003]. It may thus be that lateral and/or stratigraphic variations of quartz content within this unit are significant and do not warrant simply excluding the outcropping areas when calculating production rates. Furthermore, we stress that despite the potentially large deviations in actual erosion rates for at least two of our samples, these additional uncertainties do not affect our conclusions because the erosion rates would change by only ~0.1 mm yr^{-1}. Therefore, we did not exclude these areas in the production-rate calculation and note that the uncertainties of the above samples are higher than for the other samples and as indicated by the analytical uncertainties.

[18] We applied shielding corrections to the pixel-based production rates due to topography and the present-day ice and snow cover, but we did not consider vegetation coverage. Topographic shielding was calculated with the DEM and followed *Dunne et al*. [1999], whereas ice cover shielding (production rate set to zero) was based on present-day glacier outlines from the Randolph Glacier Inventory [*Arendt et al*., 2012]. Snow cover shielding in the Himalaya is difficult to constrain due to the lack of adequate ground-based measurements. Previous studies from the Himalaya have therefore generally neglected snow cover shielding, although studies from other high-mountain regions, e.g., the Swiss Alps [*Wittmann et al*., 2007; *Norton et al*., 2011], show that snow cover shielding can be significant. Because of the lack of suitable data on snow depths, a functional relationship with elevation or a calibrated physically based snow cover model [e.g., *Schildgen et al*., 2005] could not be used. Here we employed a simple phenomenological approach that is based on remote sensing observations of snow cover durations and typical annual cycles of snow depth, adjusted to the available data from field studies in the Himalaya (see supporting information). Our intention for this rather crude approach is to obtain a first-order estimate of snow cover shielding and to assess how sensitive our results are to this factor.

3.2. Hydromorphologic Analyses

3.2.1. Rationale

[19] Traditional morphologic measures of topography include hillslope angles or catchment relief [e.g., *Ahnert*, 1970; *Pinet and Souriau*, 1988; *Milliman and Syvitski*, 1992; *Summerfield and Hulton*, 1995]. In landscapes where fluvial incision is so rapid that soil production and diffusive hillslope transport are barely able to keep up with the downcutting of rivers, hillslopes steepen and approach a threshold angle that is determined by the strength of the rock mass [*Schmidt and Montgomery*, 1995]. Beyond this threshold, changes in hillslope erosion rates are thought to be expressed through landslide frequency [*Burbank et al*., 1996], whereas hillslope angles remain constant and cannot serve as a measure of erosion rates anymore [*Montgomery and Brandon*, 2002]. Because in such "threshold" landscapes rates of fluvial incision and hillslope mass wasting are argued to be tightly coupled, the morphology of river channels, instead of hillslopes, has been suggested to be more sensitive to erosion rate variations [*Ouimet et al*., 2009; *DiBiase et al*., 2010].

[20] The typical form of a river channel that is developed in an area of uniform climate, lithology, and rock uplift is the so-called graded profile, where the local slope, S, of a river can be cast as a power law function of the upstream area, A [*Hack*, 1957; *Flint*, 1974]:

$$S = k_s A^{-\theta} \tag{1}$$

[21] The exponent θ is usually referred to as the concavity index and the factor k_s as the channel steepness index, which gives a measure of the steepness of the fluvial part of a landscape independent of upstream area [e.g., *Wobus et al*., 2006]. Because k_s and θ are strongly correlated [*Wobus et al*., 2006], for comparison purposes, it has become common practice to normalize the channel steepness index (k_{sn}) with a reference concavity (θ_{ref}) that is either taken as the arithmetic mean of the observed concavity values in the region [e.g., *Snyder et al*., 2003] or set to a value (usually $\theta_{ref} = 0.45$) that is derived from theoretical considerations [e.g., *Whipple and Tucker*, 1999].

[22] The channel steepness index is an appealing geomorphic metric because it can be linked to the steady state longitudinal form of rivers as predicted by the stream-power family of models [e.g., *Howard and Kerby*, 1983; *Whipple and Tucker*, 1999] and used to infer spatial patterns of rock uplift [e.g., *Kirby and Whipple*, 2012]. Such inference, however, requires uniform climatic conditions in a given region, which allows substituting discharge with drainage area in the governing equations of the stream-power model. In many mountainous regions this is not the case due to orographic forcing of precipitation [e.g., *Roe*, 2005], which may result in precipitation and thus discharge gradients [e.g., *Bookhagen and Burbank*, 2006, 2010]. To better capture this orographic modulation of discharge, some studies [e.g., *Burbank et al*., 2003; *Bookhagen and Strecker*, 2012] have therefore preferred to use specific stream power, ω, within a channel to approximate its erosional capacity [e.g., *Bagnold*, 1977]:

$$\omega = \rho_w g Q S / W \tag{2}$$

where ρ_w is the fluid density, g is gravitational acceleration, Q is discharge, and W is channel width. Here we determined for all studied catchments catchment-averaged values of hillslope angle, local relief, channel steepness index, and specific stream power. In the following we briefly describe how we measured

these parameters. For the sake of brevity, we omit a detailed treatment of each step in the analysis and instead refer to the supporting information for more details and to previous studies and reviews [*Wobus et al*., 2006; *Perron and Royden*, 2012; *Bookhagen and Strecker*, 2012].

3.2.2. Topographic Data

[23] We analyzed the topography of the study area with a 90 m resolution Shuttle Radar Topography Mission digital elevation model (DEM) using MATLAB™ and the TopoToolbox v2 [*Schwanghart and Scherler*, 2014]. River channels and corresponding upstream areas were derived with a steepest descent flow-routing algorithm, with local minima (sinks) traversed along a least-cost path and their corresponding sills "carved" to minimize distortions of the true channel network [*Soille et al*., 2003]. Because channel-morphologic indices, such as channel steepness (see below), are sensitive to variations in local slope [*Wobus et al*., 2006], we smoothed the elevation data within the channels with a moving-average window of 1 km length. Flow paths were derived in topologically descending order, which ensures that the smoothing does not cross tributary confluences and thus avoids artificially large values of channel slopes in such places.

3.2.3. Hillslope Angles and Local Relief

[24] Hillslope angles for each pixel in the DEM were computed as the steepest centered-difference gradient between the eight neighboring pixels (four possible triplets). For calculating catchment-averaged values, we masked out the ridge lines as well as the valley bottoms with a buffer of 1 pixel (90 m) around the ridge and channel pixels. Local relief is defined as the maximum elevation range within a certain area [*Ahnert*, 1970]. As such, it is a scale-dependent metric that, depending on the length scale over which relief is measured, relates to different morphological aspects of the topography [e.g., *Hurtez et al*., 1999]. We measured local relief for each pixel in the DEM as the maximum elevation range within circular windows of 5 km radius. This length scale roughly corresponds to the channel-ridge line spacing of second- and third-order watersheds in our study area.

3.2.4. Normalized Channel Steepness Index

[25] In most studies of channel steepness, values for k_s and θ in equation (1) are derived from fitting a straight line to log-transformed slope and area data that are obtained from a DEM [e.g., *Wobus et al*., 2006]. An alternative way to measure k_s and θ is to transform the horizontal coordinate (distance) of channel elevation data by upstream integration and fitting a straight line to what has been called a χ plot [*Harkins et al*., 2007; *Perron and Royden*, 2012]. Here we used and compared both approaches and refer to them as slope-area regression and the integral method, respectively. First, we determined θ for each of the studied catchments by minimizing the residuals of χ and a straight line [*Perron and Royden*, 2012]. Because the mean ($\pm 1\sigma$) θ of all sampled tributary catchments (0.42 ± 0.12; 0.44 ± 0.12 when excluding previously glaciated tributaries) is close to the commonly used value of 0.45 [e.g., *Ouimet et al*., 2009; *DiBiase et al*., 2010; *Cyr et al*., 2010], we also used 0.45 as our reference concavity, θ_{ref}, to facilitate comparison of our data with previous studies. We then calculated normalized channel steepness indices (k_{sn}) for 1 km long channel reaches with the slope-area approach. Catchment-averaged k_{sn} values were derived from the arithmetic mean ($\pm 1\sigma$) of all channel reaches that have upstream areas $>1\,\mathrm{km}^2$, reflecting the transition from fluvial channels to colluvial channels and hillslopes [*Lague and Davy*, 2003]. In the case of presently ice-covered catchments, we masked out valleys that are occupied by glaciers. We further calculated k_{sn} with the integral method using the entire ice-free drainage network of a catchment (upstream areas $>1\,\mathrm{km}^2$) and the same θ_{ref}.

3.2.5. Specific Stream Power

[26] We computed specific stream power, ω, from equation (2) for the same 1 km averaged reaches that we also used for determining k_{sn}. To make ω a function of Q and S only, we used a width-discharge scaling relationship of the form $W = k_w Q^b$, with k_w and b being empirical parameters. Although channel width may also vary with S [e.g., *Finnegan et al*., 2005] and no single parameter pair is able to fit all observations, we set b to 0.5, which is a typical value in both alluvial and bedrock channels [e.g., *Montgomery and Gran*, 2001; *Wohl and David*, 2008; *Kirby and Whipple*, 2012]. While measurements from satellite imagery to the east corroborate the 0.5 exponent as a general average, there exists considerable width variability between contrasting lithologic and tectonic regimes that cannot currently be accounted for in smaller order streams [*Fisher et al*., 2013]. We noted larger channel width variability along the main stems during our field work. We set the scaling factor k_w to one, as it merely reflects a constant of proportionality and does not influence any relative differences between the studied catchments. In this study, we neglected the effects of erosion thresholds and event-scale discharge variations [e.g., *Tucker and Bras*, 2000; *Tucker*, 2004; *Lague et al*., 2005; *DiBiase and Whipple*, 2011] and instead focused on mean annual discharge.

[27] We calculated the mean annual discharge, Q, for each pixel in the DEM by routing estimates of annual runoff through the drainage network. Although a significant amount of precipitation can be temporally stored as groundwater, even in steep landscapes such as the Himalaya [e.g., *Andermann et al*., 2012], we assume that over annual timescales, no net loss occurs through subsurface flow and that all runoff enters the rivers. Because the majority of precipitation in the Yamuna catchment occurs during summer [*Jha et al*., 1988; *Bookhagen and Burbank*, 2010], monsoonal rainfall is the most important contribution to discharge. However, as shown by the remote sensing-derived snow cover durations (Figure S1), the contribution of snow melt to discharge could be significant in some tributaries. Therefore, we compared two different estimates of annual runoff that have been obtained by *Bookhagen and Burbank* [2010]. The first one comprises runoff that is entirely derived from annual rainfall as provided by the 2B31 data set of the Tropical Rainfall Measuring Mission (TRMM) [*Huffman et al*., 2007], calibrated to rain- and river-gauging data throughout the Himalayas and the Gangetic foreland. The second estimate of annual runoff is based on TRMM data, as well as modeled estimates of snow melt and evapotranspiration. The snow melt contribution to discharge is computed with a degree-day snowmelt model based on field-calibrated remote sensing data for snow-covered area, land-surface temperature, and DEM-derived solar radiation. Evapotranspiration is also based on remote sensing data and included into the hydrologic model and flow routing. For more detailed information, we refer to *Bookhagen and Burbank* [2010].

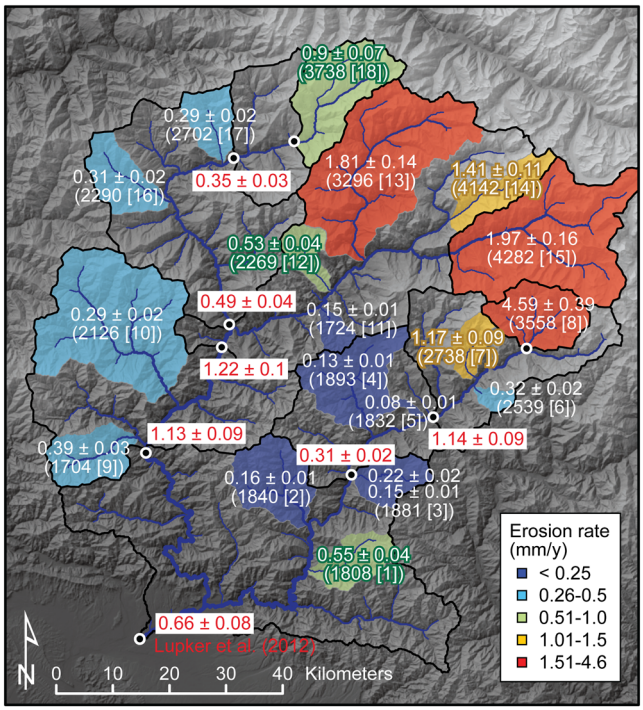

Figure 4. ^{10}Be-derived erosion rates for tributary catchments (colored polygons and white bold numbers) and trunk stream samples (black-outlined polygons and red bold numbers), including sample by *Lupker et al.* [2012]. Numbers in parenthesis refer to mean tributary elevations, and catchment IDs are given in square brackets (cf., Tables 1–3).

4. Results

4.1. ^{10}Be-Derived Erosion Rates

[28] The ^{10}Be-derived catchment-averaged erosion rates are shown in Table 2 and Figure 4. To first order, tributaries that are located in the LH, at elevations <3000 m, are eroding with rates lower than 0.5 mm yr^{-1}, whereas catchments in the HH that extend to higher elevations (>3000 m) have higher erosion rates. We obtained the highest erosion rates (>1.5 mm yr^{-1}) in the uppermost reaches of the Tons and Yamuna valleys. Our highest tributary in the Yamuna Valley with a mean elevation of ~3500 m yielded an erosion rate of 4.6 ± 0.4 mm yr^{-1}. In contrast to these high rates, much lower erosion rates (~0.1–0.2 mm yr^{-1}) are found only 30–40 km farther downstream at mean elevations of ~1800 m. In the headwaters of the Tons Valley, the highest erosion rates, close to 2 mm yr^{-1}, stem from tributaries that had previously been glaciated (#13–15). Along the lower parts of the Pabbar and Tons Valleys, tributary erosion rates are also low (~0.3 mm yr^{-1}) but slightly higher than along the central part of the Yamuna Valley. Compared to the central parts of the Tons and Yamuna Valleys, the lowest-located tributaries appear to have slightly higher erosion rates, which is more pronounced in the Yamuna Valley (Figure 4). Finally, the catchment-averaged erosion rates of the main stem samples span from ~0.3 mm yr^{-1} to ~1.2 mm yr^{-1}, with opposing downstream trends in the Yamuna and Pabbar-Tons valleys.

4.2. Hillslope Angles and Local Relief

[29] As already indicated by the swath profile shown in Figure 2, catchment-averaged hillslope angles are generally high, in most cases above 25°, and rather uniform across the sampled tributary catchments (Table 3). The variance of hillslope angles within the catchments is generally high (mean 1σ = 8°, i.e., 28%). Compared to hillslope angles, 5 km radius local relief shows smaller variance within all sampled catchments, i.e., lower standard deviations (mean 1σ = 201 m, i.e., 11%), and the catchment-averaged values cover a wider range between the sampled catchments. The highest local relief is seen within the partly ice-covered catchments (#13–15) in the HH where they also show the highest variance. The lowest local relief values are found in catchments that are located in the LH. The spatial pattern of local relief and the other parameters is depicted in Figure 5 along a N45° projected distance from the MBT at the Tons-Yamuna confluence. At a distance of ~10–40 km from the MBT, catchment-averaged local relief is between ~1.5 and 1.8 km, between ~40 and 55 km distance, local relief is <1.5 km, and at yet greater distances it increases quite abruptly to values mostly >2 km.

4.3. Normalized Channel Steepness Index

[30] Normalized channel steepness indices, k_{sn}, of the sampled catchments are between 100 and 311 m$^{0.9}$ when determined by the integral method for each catchments' entire drainage network. These values are in close agreement with catchment-averaged k_{sn} values obtained by the slope-area approach for 1 km long channel reaches (Table 3 and Figure 5c). For the tributaries with well-developed knickpoints (#1, 4, 10) and for one of the presently ice-covered tributaries (#14), the k_{sn} values derived by the two methods diverge by up to 25% (cf., Figure 3). The highest-reaching tributaries (#8, 13–15, 18) exhibit the largest variation in k_{sn} within their catchments, which is expressed by large standard deviations of reach-scale k_{sn} values and deviations from the best fit linear χ plot (Figure 5a). The trend in k_{sn} values across the range is very similar to that of local relief, with the notable exception of tributary #8, which has by far the highest local relief value but only a moderately high k_{sn} value. Good correspondence between local relief and channel steepness has been previously observed in other settings [*DiBiase et al.*, 2010] and is shown in map view in Figure 6. This map view also depicts the greater channel steepness of the Tons River compared to the Pabbar and Yamuna Rivers and shows that this corresponds to higher local relief, hence a generally deeper incised valley.

4.4. Specific Stream Power

[31] Catchment-averaged specific stream power values, ω, vary between ~500 and ~1500 W m^{-2} and show high variability within the catchments, with standard deviations exceeding average values in several catchments (Table 1 and Figure 5d). Interestingly, ω is quite similar for discharge that is either based on rainfall only or additionally considers evapotranspiration and snowmelt. As would be expected, the largest differences in ω derived from discharge based on rainfall only versus rainfall, evapotranspiration, and snowmelt are found for catchments that reach to high elevations, with tributary #14 having the greatest amount of

Table 3. Catchment-averaged Hydromorphometric Parameters

ID[a]	Hillslope angle[b] (°)	5 km radius local relief (m)	ω(Q=R)[c] (W m^{-2})	ω(Q=R-ET+M)[d] (W m^{-2})	k_{sn} (S-A regr.)[e] (m$^{0.9}$)	k_{sn} (integr. method)[f] (m$^{0.9}$)	m/n[g]
			Yamuna tributaries				
1	27.9 ± 6.2	1690 ± 165	873 ± 645	833 ± 330	168 ± 56	158 ± 2	0.36
2	27.5 ± 6.6	1577 ± 196	840 ± 585	809 ± 521	161 ± 45	149 ± 2	0.57
3	25.8 ± 7.2	1542 ± 113	818 ± 532	754 ± 570	167 ± 54	161 ± 1	0.47
4	24.6 ± 8.4	1382 ± 186	641 ± 529	600 ± 511	115 ± 48	100 ± 2	0.70
5	25.2 ± 7.4	1345 ± 18	604 ± 159	593 ± 125	144 ± 22	146 ± 1	0.20
6	31.4 ± 8.1	2161 ± 136	1285 ± 305	1352 ± 325	212 ± 40	218 ± 3	0.36
7	33.1 ± 8.2	2282 ± 211	1229 ± 367	1174 ± 345	217 ± 57	213 ± 2	0.49
8	30.8 ± 8.9	2597 ± 424	1504 ± 736	1641 ± 887	260 ± 87	264 ± 2	0.45
			Tons tributaries				
9	28.3 ± 6.9	1616 ± 112	1163 ± 1647	1025 ± 317	164 ± 55	132 ± 1	0.56
10	27.8 ± 7.1	1745 ± 210	1011 ± 752	967 ± 683	181 ± 63	161 ± 1	0.42
11	27.0 ± 8.3	1287 ± 168	559 ± 202	521 ± 183	101 ± 27	112 ± 1	0.37
12	32.8 ± 7.9	2086 ± 215	1009 ± 437	964 ± 439	187 ± 68	182 ± 2	0.46
13	30.4 ± 9.6	2226 ± 223	1454 ± 1731	1443 ± 1322	264 ± 106	267 ± 1	0.32
14	33.0 ± 9.4	2432 ± 399	1156 ± 1195	1513 ± 1678	250 ± 165	311 ± 6	-0.40
15	30.3 ± 9.5	2375 ± 352	1240 ± 1047	1303 ± 1282	261 ± 129	279 ± 2	0.29
			Pabbar tributaries				
16	23.0 ± 6.5	1308 ± 90	567 ± 244	538 ± 203	125 ± 28	126 ± 1	0.37
17	27.3 ± 7.8	1919 ± 292	821 ± 428	788 ± 321	174 ± 43	189 ± 2	0.51
18	28.7 ± 9.0	2100 ± 192	1198 ± 1405	1220 ± 824	244 ± 97	252 ± 2	0.24
			Main Stems				
Y1	29.5 ± 8.8	2237 ± 405	1468 ± 1313	1514 ± 1336	235 ± 85	234 ± 1	0.39
Y2	27.8 ± 8.7	1899 ± 495	1122 ± 1067	1129 ± 1097	191 ± 87	186 ± 1	0.48
P1	27.1 ± 8.7	2080 ± 217	1167 ± 1028	1172 ± 685	237 ± 78	239 ± 1	0.32
P2	26.8 ± 8.0	1865 ± 328	1032 ± 982	947 ± 574	196 ± 78	194 ± 1	0.46
T1	28.5 ± 8.8	2054 ± 381	1206 ± 1552	1171 ± 1142	221 ± 104	219 ± 1	0.39
T2	28.6 ± 8.5	1978 ± 366	1187 ± 1699	1145 ± 1475	211 ± 96	199 ± 1	0.43
Y3	28.1 ± 8.5	1857 ± 417	1138 ± 1856	1134 ± 1996	194 ± 93	166 ± 1	0.50

[a] ID = Tributary number shown in Fig.1; mainstem sample abbreviations: Y = Yamuna, T = Tons, P = Pabbar.
[b] Values in columns 2-6 refer to mean ± 1σ.
[c] Mean annual discharge (Q) based in TRMM-derived annual rainfall (R).
[d] Q based on TRMM-derived R, as well as modeled evapotranspiration (ET) and snowmelt (M).
[e] k_{sn} = normalized steepness index; based on slope (S)-area (A) regression. Statistics derived from 1-km-long reaches within each catchment.
[f] k_{sn}, based on integral method. Error refers to the uncertainty in the k_{sn} value from fitting the χ-transformed elevation data with a linear model.
[g] m/n = concavity index; derived by least-squares regression from χ-transformed stream network of tributary.

snowmelt-derived runoff (Table 1). The general trend in ω across the mountain range, however, is very similar to that of local relief and k_{sn}, with lowest specific stream power at a distance of ~40 to 55 km from the MBT (Figure 5d).

5. Analysis

5.1. Correlation Between Erosion Rates and Morphologic Parameters

[32] Apart from catchment-averaged hillslope angles, the ^{10}Be-derived erosion rates from tributary catchments correlate positively with the studied morphometric parameters and appear independent of lithological differences (Figure 7). The increase of ^{10}Be-derived erosion rates with catchment-averaged local relief, k_{sn}, and ω is best described with a power law. The main differences lie within the degree of nonlinearity in the best fit relationships. For example, considering the entire tributary data set, erosion rates scale with local relief and ω, raised to a power of ~9 and 6, respectively. These values reduce to ~5 and 3, when ignoring the sample with the highest erosion rate (tributary #8), but still reflect considerable nonlinear relationships. The best fit relationship between ^{10}Be-derived tributary erosion rates and k_{sn} depends on the choice of k_{sn}. When comparing erosion rates with the catchment-averaged k_{sn} values that were derived by the slope-area approach, the relationship is similarly nonlinear as for the ω data, with a scaling exponent of ~6 or 4 when ignoring the sample from tributary #8. However, using the k_{sn} values derived from the integral method and ignoring the sample from tributary #8 result in a smaller power law exponent (Figure 8), particularly due to the high-erosion rate sample from the previously glaciated tributary #14 that has the highest k_{sn} value. In fact, this relationship can be equally well described with a linear model that has a negative y intercept. Considering the entire tributary data set and k_{sn} values derived from the integral method, the coefficient of determination is the lowest among the three examined parameters ($R^2 = 0.47$ for both the linear and power law models; not shown).

5.2. Comparison of Predicted Erosion Rates with ^{10}Be-Derived Main Stem Erosion Rates

[33] Based on our data set of tributary ^{10}Be-derived erosion rates and the functional relationships with the examined parameters (local relief, k_{sn}, ω), we predicted catchment-averaged erosion rates for the areas upstream of our main stem samples. Because the functional relationships we used are tied to catchment-averaged values, we also computed catchment-

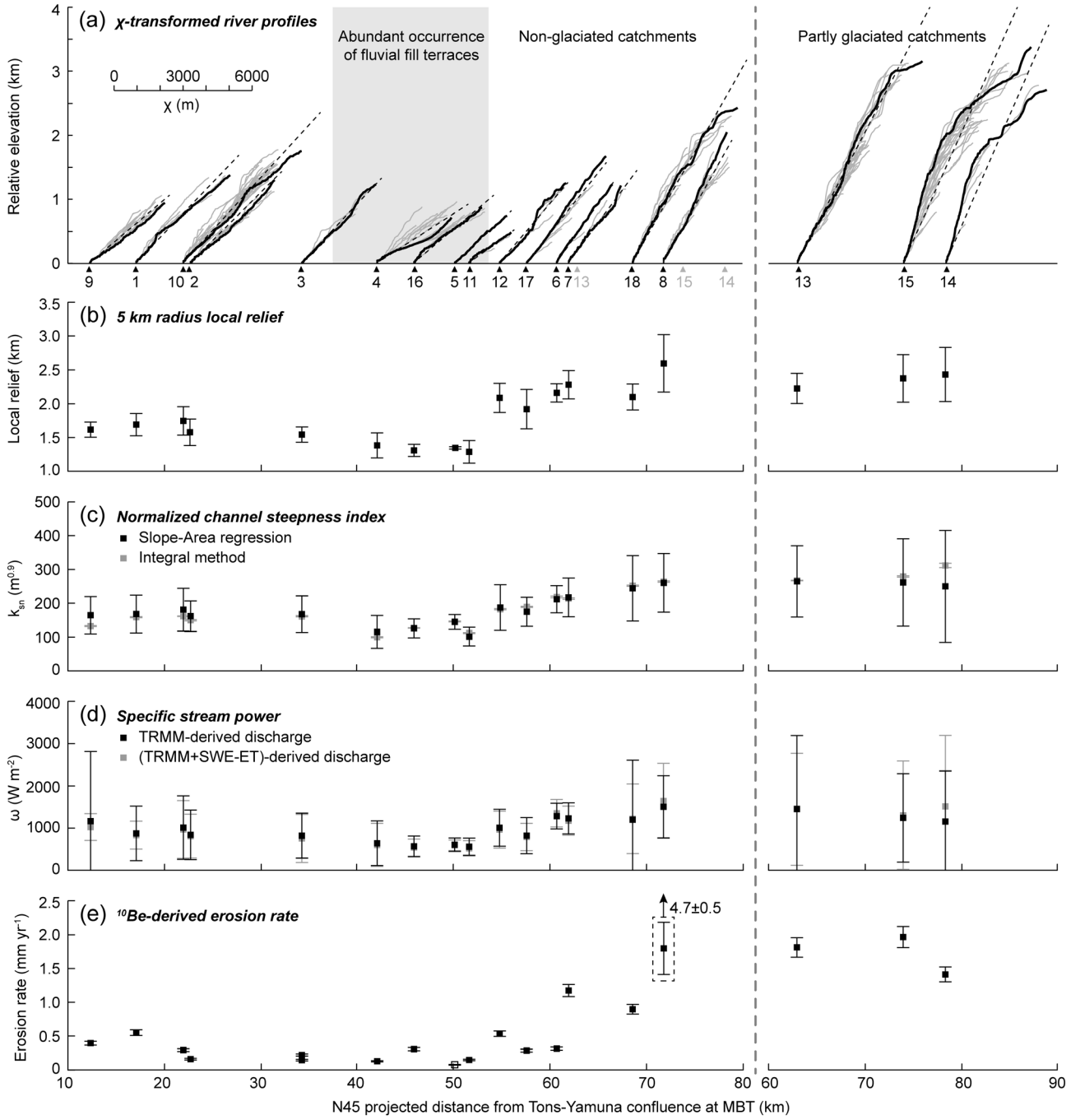

Figure 5. Catchment characteristics of the sampled tributaries. (a) χ-transformed longitudinal river profiles ($A_0 = 1\,\mathrm{km}^2$, $\theta_{ref} = 0.45$). The drainage network of each tributary consists of a trunk stream (black) and tributaries (gray), which together have been fitted with a linear model (dashed). The slope of the linear fit is proportional to k_{sn}. Note that x axis shows χ with units of meters (scale bar in upper left corner), but position along x axis refers to N45-projected distance of tributary outlets from the Tons-Yamuna confluence at the Main Boundary Thrust (MBT), which is parallel to the trend of the middle Yamuna and Tons rivers and approximately parallel to the trend of the profile in Figure 2. Tributaries with glacial signature in river profile are shown separately on the right side. (b) 5 km radius local relief. (c) Normalized channel steepness index, k_{sn} ($\theta_{ref} = 0.45$), derived by slope-area regression and the integral method. (d) Specific stream power, ω, based on different discharges. (e) ^{10}Be-derived erosion rates. Error bars reflect (Figures 5b–5d) 1σ variability of values within each catchment and (Figures 5e) 2σ analytical and model-based uncertainties.

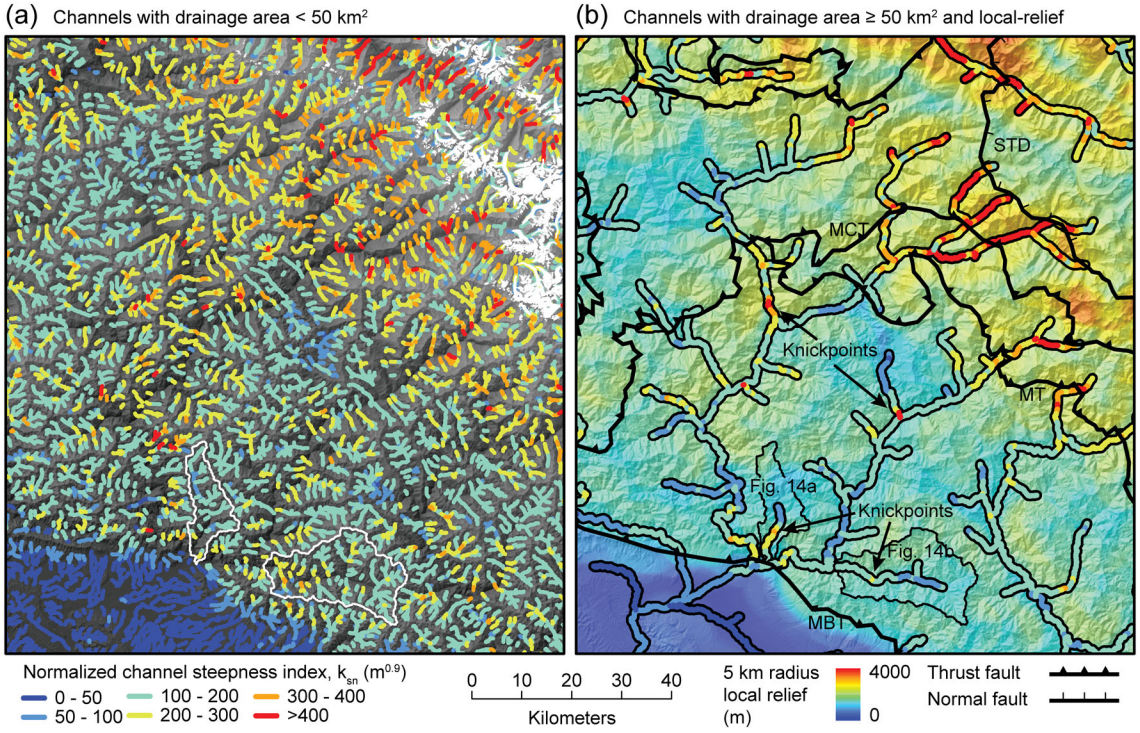

Figure 6. Normalized channel steepness index for 1 km long channel reaches. (a) Channels with drainage area $<50\,km^2$. White areas give present-day ice coverage. (b) Channels with drainage area $\geq 50\,km^2$. Background shows 5 km radius local relief. Black bold lines indicate fault traces; MBT = Main Boundary Thrust, MT = Munsiari Thrust, MCT = Main Central Thrust, STD = South Tibetan Detachment. Catchment outlines near MBT refer to lowermost Yamuna tributaries upstream of MBT with pronounced knickpoints (see Figure 14).

averaged values in the case of the main stem samples (Table 3). Note that the uncertainties in the predicted erosion rates we provide are based on the 95% prediction bounds of the functional relationship and do not reflect the variance of the independent variables, which is usually substantial (Table 3). In the case of local relief, we calculated the independent variables by averaging local relief over all pixels in the upstream areas. In the case of k_{sn} and ω, we calculated the independent variables by averaging k_{sn} and ω over all 1 km long channel reaches in the upstream areas.

[34] In general, the predicted main stem erosion rates are broadly distributed and have high uncertainties when using the relationships derived from taking the entire ^{10}Be tributary data set into account (Table 4). A broad distribution is particularly pronounced in cases where the relationship is highly nonlinear. When using the functional relationships derived by excluding the sample from tributary #8, the predicted erosion rates derived from the different metrics have relatively similar values and are on average not far from the ^{10}Be-derived erosion rate (Table 4 and Figure 9), but there are some exceptions. The ^{10}Be-derived erosion rates are lower than all the predicted values for the samples Y2 and P1 and higher for samples T1 and T2. Samples Y1, P2, and Y3 are very close to at least two of the predicted values. There is, however, no clear sign as to whether one of the relationships tends to systematically predict higher or lower erosion rates compared to the other and no clearly better performance of any of the parameters to predict the ^{10}Be-derived erosion rates. It should be noted that the variance of the predicted erosion rates in the upstream areas differs substantially between the different predictors. Local relief, which by its definition is already a spatially averaged metric that does not tend to produce extreme values, shows generally the smallest variance (Table 3), whereas much larger variances exist for k_{sn} and ω because they strongly depend on local channel slopes. However, the high nonlinearity in some of the functional relationships with the parameters results in significantly greater variance of the predicted erosion rates than the catchment-averaged value would suggest.

6. Discussion

6.1. Reliability of ^{10}Be-Derived Tributary Erosion Rates

[35] In general, the ^{10}Be-derived tributary erosion rates are relatively low (~0.1–0.5 mm yr^{-1}) over most of the LH, that is, at elevations <3000 m, whereas they are higher (~1–2 mm yr^{-1}) in the HH, at elevations >3000 m. Although the good correlation between erosion rates and catchment-averaged local relief, k_{sn}, and ω provides confidence in the relative differences we observe between our samples, this does not preclude systematic biases that could occur due to model assumptions being violated in the LH and HH to a different degree. We therefore first discuss the possibilities for any systematic biases and their potential impact.

[36] Systematic underestimation of erosion rates can occur if most erosion is due to infrequent landslides. This issue has been addressed in numerical studies, which suggest that for an increasing contribution of landslides to total erosion, successively larger catchments need to be sampled to ensure

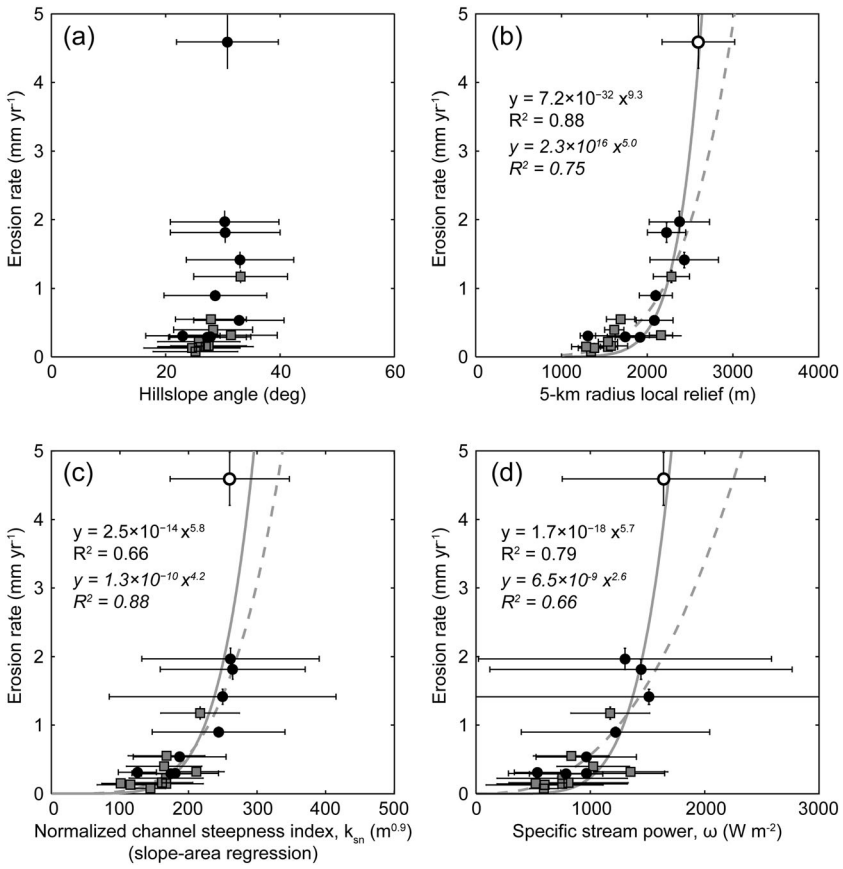

Figure 7. Relationship between ^{10}Be-derived erosion rates and (a) mean hillslope angles, (b) 5 km radius local relief, (c) normalized channel steepness index, k_{sn}, and (d) specific stream power, ω, based on annual runoff through rainfall (minus evapotranspiration) and snowmelt. Squares and circles denote catchments predominantly developed in LH metasedimentary rocks and LH/HH crystalline rocks, respectively. Equations and lines refer to least squares fit of all data points (regular font, solid line) and all data points except for the high-erosion rate sample denoted by a hollow circle (italic font, dashed line). The x axis error bars give 1σ standard deviations of values within each catchment.

sufficient mixing of landslide and nonlandslide material and avoid this bias [*Niemi et al*., 2005; *Yanites et al*., 2009]. Although it is difficult to definitely exclude such bias, we note that we do not observe any systematic variation of erosion rates with catchment size that could be interpreted to reflect a bias due to landsliding (Table 2). The impact of landslides on cosmogenic-nuclide concentrations in fluvial sediment depends, besides mixing within the channel, also on the depth and frequency of landslides [*Yanites et al*., 2009] and thus whether landslides remain shallow or affect bedrock. Although it is often stated that deep-seated bedrock landsliding is a dominant erosion mechanism in the Himalaya [e.g., *Burbank et al*., 1996; *Gabet et al*., 2004; *Lupker et al*., 2012], the empirical basis for this assumption is rather weak. There has been, to our knowledge, no study that tried to quantify the contribution of deep-seated landsliding to total erosion in different parts of the orogen. At least in the humid, vegetated, and soil-covered areas that make up the LH and some parts of the HH, we have seen more evidence for frequent shallow landsliding as compared to deep-seated bedrock landsliding, consistent with observations following

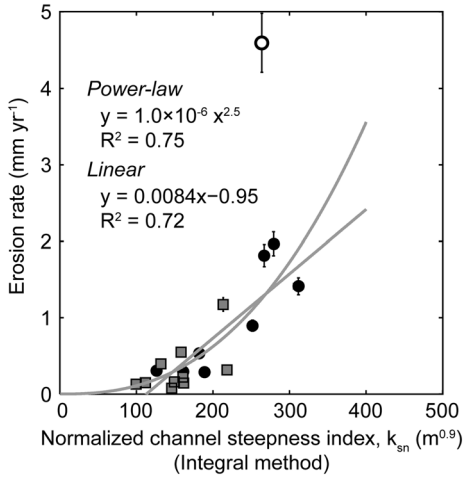

Figure 8. Correlation between ^{10}Be-derived erosion rates and normalized channel steepness index, k_{sn}, determined with the integral method. High-erosion rate sample (hollow circle) was omitted from least squares fit.

Table 4. Predicted and ^{10}Be-Derived Catchment-Averaged Erosion Rates for Main Stem Samples

ID	Predicted Erosion Rates (mm yr^{-1}), Based on Catchment-Averaged Values of[a]:								
	5 km radius local relief		Specific stream power		k_{sn}, slope-area regr.		k_{sn}, integral method		
Power law exponent[b]	9.3	5.0	5.7	2.6	5.8	4.2	1 (linear)	2.5	^{10}Be-Derived Erosion Rate (mm yr^{-1})
Y1	1.1 ± 0.9	*1.1 ± 0.7*	1.8 ± 1.2	*1.4 ± 0.9*	1.3 ± 1.5	*1.1 ± 0.5*	*1.0 ± 0.7*	*0.9 ± 0.7*	1.14 +/− 0.09
Y2	0.2 ± 0.8	*0.5 ± 0.7*	0.4 ± 1.1	*0.7 ± 0.8*	0.4 ± 1.4	*0.5 ± 0.5*	*0.7 ± 0.7*	*0.6 ± 0.7*	0.31 +/− 0.02
P1	0.5 ± 0.8	*0.8 ± 0.7*	0.5 ± 1.1	*0.8 ± 0.8*	1.4 ± 1.5	*1.1 ± 0.5*	*1.0 ± 0.7*	*1.0 ± 0.7*	0.35 +/− 0.03
P2	0.2 ± 0.8	*0.5 ± 0.7*	0.2 ± 1.1	*0.5 ± 0.8*	0.4 ± 1.5	*0.5 ± 0.5*	*0.7 ± 0.7*	*0.6 ± 0.7*	0.49 +/− 0.04
T1	0.5 ± 0.8	*0.7 ± 0.7*	0.4 ± 1.1	*0.7 ± 0.8*	0.8 ± 1.5	*0.8 ± 0.5*	*0.9 ± 0.7*	*0.8 ± 0.7*	1.22 +/− 0.10
T2	0.3 ± 0.8	*0.6 ± 0.7*	0.4 ± 1.1	*0.7 ± 0.8*	0.7 ± 1.5	*0.7 ± 0.5*	*0.8 ± 0.7*	*0.7 ± 0.7*	1.13 +/− 0.09
Y3	0.2 ± 0.8	*0.5 ± 0.7*	0.4 ± 1.1	*0.7 ± 0.8*	0.4 ± 1.4	*0.5 ± 0.5*	*0.7 ± 0.7*	*0.6 ± 0.7*	0.66 +/− 0.08

[a]Italic number corresponds to relationships derived without the high-erosion rate data point marked in Figure 7 as suspected outlier.
[b]Exponents relate to the functional relationships given in Figures 7 and 8.

the 1999 M_w 6.4 Chamoli earthquake [*Barnad et al*., 2001] and the 2005 M_w 7.6 Kashmir earthquake [*Owen et al*., 2008]. We thus assume that our choice of catchment sizes is sufficient to account for erosion by landslides in the LH.

[37] Further potentially systematic biases may be introduced due to the neglected effect of shielding through vegetation, which is generally higher in the LH compared to the HH and our simple model for snow cover shielding, which is higher in the HH compared to the LH. Any neglected shielding causes actual production rates to be lower than assumed, which would result in lower actual erosion rates. However, shielding by vegetation is most likely minor and below 5% even in dense forests [*Cerling and Craig*, 1994], suggesting that this bias, although most likely present, is small compared to other uncertainties. Our applied snow cover shielding has negligible effect on most LH samples (<2%) but accounts for 10–20% lower erosion rates for the HH samples compared to erosion rates calculated without any snow cover shielding (Table 2 and Table S1). Although it is difficult to assess the validity of our snow cover shielding factors, we note they are similar in magnitude to those based on snow-depth measurements for high-altitude catchments in the European Alps [*Wittmann et al*., 2007; *Norton et al*., 2011]. Ice cover shielding occurs in only two of our tributaries (#14 and #15 and Table 1) but did not result in an unusual low concentration as has been observed in central Nepal [*Godard et al*., 2012], for example. The contribution of glacial sediments from the last glacial episode to modern river sediments is hard to evaluate, and more dedicated studies have shown that inherited concentrations can vary substantially [*Wittmann et al*., 2007]. Thus, we acknowledge that this results in greater uncertainties for erosion rates from previously glaciated catchments (#13–15, #18) but likely no systematic and, given the limited reconstructed ice extent during the late Pleistocene [*Scherler et al*., 2010], no significant bias.

[38] Systematic underestimation of erosion rates can also occur due to quartz enrichment by selective dissolution in vertically mixed soils [*Small et al*., 1999]. This effect can be important where chemical weathering rates are high and erosion rates are low [*Riebe and Granger*, 2013]. *Dalai et al*. [2002] report chemical weathering rates on the order of ~0.04 mm yr^{-1} from carbonates and ~0.01 mm yr^{-1} from silicates in the Yamuna catchment. These values are comparable to chemical erosion rates from Central Nepal [*France-Lanord et al*., 2003] and suggest that chemical erosion rates are only a small fraction of physical erosion rates when exposure of carbonate rocks is low [e.g., *France-Lanord et al*., 2003; *Garzanti et al*., 2007; *Tripathy and Singh*, 2010]. Because limestones and dolostones occur in the LH, where erosion rates are low, this effect could potentially be important. However, we do not observe any systematic differences in erosion rates between samples that drain LH catchments with presumably very different carbonate contents, as indicated by the mass losses from hydrochloric leaching during sample processing (Table S2).

[39] In summary, we currently see no evidence for any significant systematic bias of our ^{10}Be-derived erosion rates in the LH. However, in the very steep parts of the HH, where soils are largely absent and bedrock surfaces common, frequent rock falls, rock slides, and debris flows may lead to higher variability of concentrations with time. Moreover, infrequent deep-seated bedrock landslides [e.g., *Bookhagen et al*., 2005] pose greater uncertainties in the HH and potentially render the ^{10}Be-derived erosion rates lower than longer-term erosion rates actually are. We currently lack enough samples from the more rapidly eroding HH to ascertain if the determined erosion rate of tributary #8 is reliable or not, but we note that all other samples from the HH

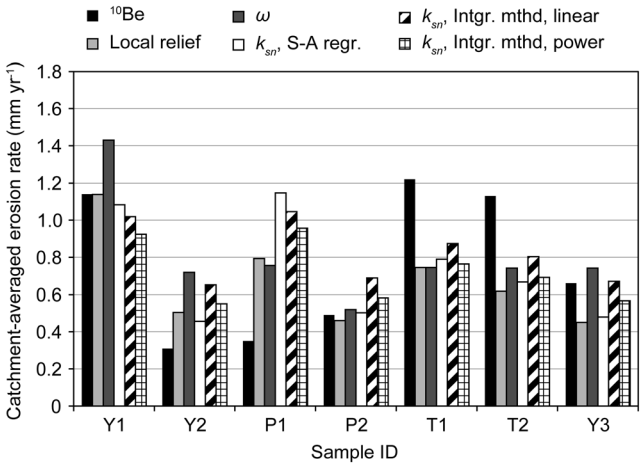

Figure 9. Comparison of ^{10}Be-derived and predicted catchment-averaged erosion rates for the main stem samples. "Power" and "linear" refer to the power law and linear equations from Figures 7c and 8, respectively. All predicted erosion rates are based on regressions of the ^{10}Be-derived tributary data without the high-erosion rate value from tributary #8.

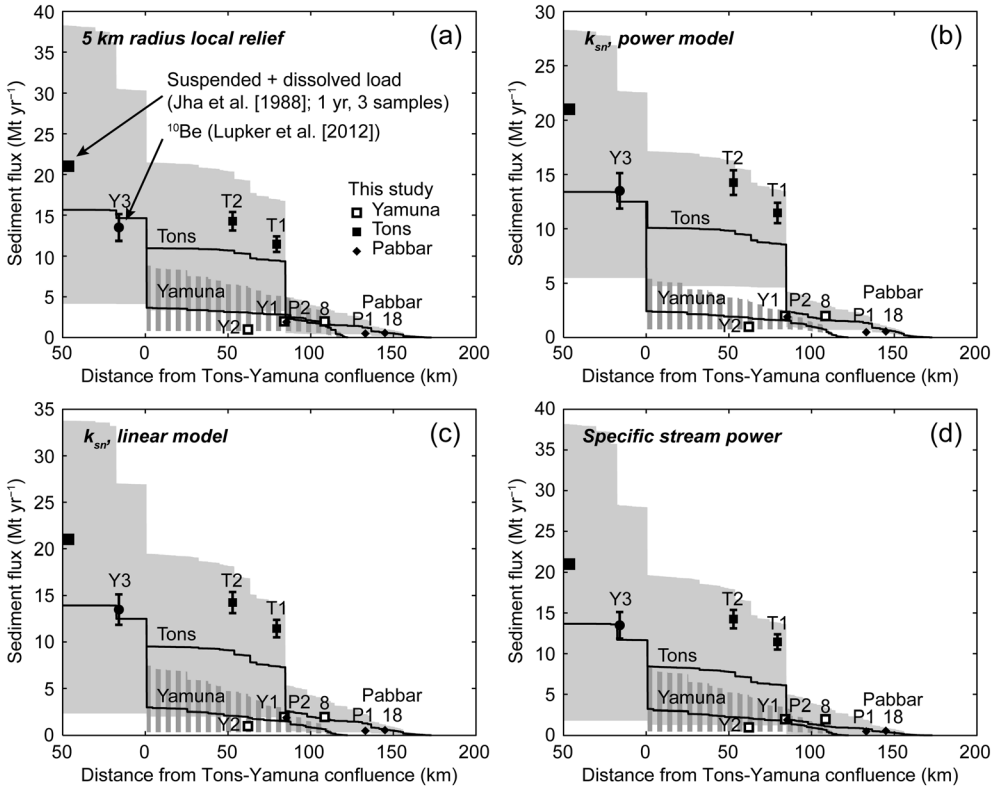

Figure 10. Downstream evolution of sediment flux based on ^{10}Be-derived erosion rates (data points) and erosion rates predicted from (a) 5 km radius local relief, (b) normalized channel steepness (k_{sn}) using the power law equation from Figure 7c, (c) k_{sn} using the linear equation from Figure 8, and (d) specific stream power. All predicted erosion rates (black lines) are based on regressions of the ^{10}Be-derived data without the high-erosion rate value from tributary #8. Gray and vertically striped areas correspond to 2σ uncertainties.

that give lower erosion rates correspond to catchments that bear clear signs of glaciation during the Pleistocene, which is not the case for the very steep catchment of tributary #8. Because the best fit of the hydromorphometric parameters to the ^{10}Be data is very sensitive to the high-erosion rate data points from the HH (Figures 7 and 8), this uncertainty poses a challenge for establishing a functional relationship that is robust over a wide range of erosion rates.

6.2. Downstream Variations of ^{10}Be-Derived Main Stem Erosion Rates

[40] The observed variation of the ^{10}Be-derived main stem erosion rates is largely within the uncertainties of the predicted erosion rates based on the tributary samples. Relatively higher discrepancies for some samples (Y2, P1, T1, T2 and Figure 9) may point to underestimation or overestimation of actual erosion rates by either the ^{10}Be concentrations or the modeled erosion rates. To shed light on this issue, we calculated the downstream variation of sediment fluxes (Figure 10) by multiplying the ^{10}Be-derived erosion rates with their corresponding upstream areas. In principle, this flux should monotonically increase, as ^{10}Be-derived erosion rates cannot be negative. However, the previously identified samples partly behave abnormally because they result in downstream decreasing sediment fluxes (#18–P1; Y1–Y2; T2–Y3), indicating that it may be the ^{10}Be signal that is spurious. Although the sample number is rather small, it is worth noting that deviation of the ^{10}Be-derived erosion rates from the modeled erosion rates is unsystematic and is not seen for all our main stem samples. This behavior makes an explanation due to, e.g., introduction of sediment with lower concentrations from deeper sources through human-induced recent gullying [e.g., *von Blanckenburg et al*., 2004] unlikely in our case, particularly as human activity increases downstream. If the abnormal concentrations were due to mixing with sands derived from the fill terraces, we would also expect a signal that varies systematically downstream and that correlates with the exposure of these terraces, which are mainly found along certain reaches of the main stem rivers (cf., Figure 5).

[41] In our calculation of erosion rates, we did not apply any correction for spatially varying quartz content. While this appears unproblematic for most of the tributary samples because of the small catchment size and mostly uniform lithology within the catchments, it could have an effect on our main stem samples. In the neighboring Alaknanda and Bhagirathi catchments, modal quartz contents of bed load from tributaries in the LH (excluding the Deoban Formation) and HH appear to vary within relatively narrow ranges (55 ± 7%, *Vance et al*. [2003]) and are similar to those from HH bedrock samples (51 ± 9%, *Ahmad et al*. [2000]), suggesting a minor, if any, systematic bias. Although variations of characteristic quartz-grain sizes in the source rocks

could also be important because smaller grains are preferentially lost during removal of meteoric ^{10}Be by hydrofluoric leaching of the samples, we do not consider this effect to be important. First, our choice of grain sizes (125–500 μm) restricts this effect to only the smallest grain sizes. Second, we did not observe any systematic differences in mass loss due to hydrofluoric leaching between samples from the LH and HH (Table S2).

[42] *Lupker et al*. [2012] related unsystematic variations of ^{10}Be concentrations in samples from large (>20,000 km^2) central Himalayan catchments to variability of sediment contributions by the main tributaries. This effect requires that distinct source areas have pronounced differences in surface elevation, which result in corresponding differences in production rates. All three studied rivers have their headwaters in significantly higher elevations (mean elevation >3000 m) than any of their tributaries farther downstream (mean elevation <3000 m; Table 1), with concurrent differences in surface-production rates (Table 2). Although sediment transport most likely occurs in all tributaries during the monsoon season, it has been observed that individual, particularly strong, and spatially restricted monsoonal storms sometimes increase the efflux of sediment from certain catchments by orders of magnitudes [*Wulf et al*., 2010]. We therefore hypothesize that the anomalous magnitudes of some main stem erosion rates may be due to nonproportional sediment supply and lack of mixing. The maximum deviation, of the ^{10}Be-derived erosion rates from the average of the predicted erosion rates, is ~60%, which may be regarded as an additional measure of uncertainty for these samples.

[43] We also computed the downstream evolution of sediment fluxes by calculating the erosion rate at every point in the DEM based on the relationships in Figures 7 and 8. In the case of k_{sn} and ω, we first generated grids by linear interpolation and smoothing of reach values with a 5 km radius moving-average filter. Before summing up upstream fluxes, negative fluxes were set to zero. Uncertainties are based on the 95% prediction bounds derived from the least squares regression. Overall, the tested parameters yield similar sediment flux curves along the main stem rivers (Figure 10), which are in good agreement with the flux derived from the sample of *Lupker et al*. [2012] near the outlet but lower than the sediment flux reported by *Jha et al*. [1988], which however is based on only three suspended and dissolved load measurements. For all parameters, the Tons River consistently has the greatest contribution to sediment yield of the Yamuna catchment, which reflects its greater total area and larger fraction of HH source areas. This dominance is the smallest for ω-based erosion rates, most likely because of the lower discharge and gentler channel slopes in the headwaters of the Tons. In contrast, for erosion rates based nonlinearly on k_{sn}, the difference is greatest, and the flux estimates for the Yamuna and Pabbar rivers are comparatively small.

6.3. Climatic Influence on the Spatial Distribution of Erosion

[44] Our analysis has shown that the ^{10}Be-derived tributary erosion rates can be equally well fitted with parameters that relate only to the topographic steepness of the catchments, i.e., local relief and normalized channel steepness index (k_{sn}), and with specific stream power (ω), which explicitly takes spatial gradients in discharge-generating precipitation into account. Moreover, ω that is calculated from discharge due to rainfall only is not substantially different from one that takes account of evapotranspiration and snowmelt (Table 1). These results suggest that twofold to threefold differences in annual runoff between the studied catchments have negligible effects on ^{10}Be-derived erosion rates. Therefore, and because in small to medium-sized tributaries discharge usually scales linearly with area, substituting discharge with area in the stream-power model appears warranted in most parts of the Yamuna catchment and leads to the generally good correlation of k_{sn} with erosion rates. However, it may still be that total annual discharge is not the appropriate hydrologic quantity in controlling fluvial incision and that a better correlation with the ^{10}Be-erosion rates can be achieved with a more detailed consideration of flow regimes. For example, if a threshold confines incision to occur only during high discharge events, then the full distribution of discharge events has to be considered [e.g., *Snyder et al*., 2003; *Tucker*, 2004; *Lague et al*., 2005; *DiBiase and Whipple*, 2011], which may also lead to significant differences between rainfall and snowmelt-dominated regimes.

[45] The spatial coincidence of high-erosion rates with a peak in precipitation along the steep southern slope of the HH has led previous researchers to suggest a decisive role of climate on erosion and, via feedback mechanisms, also on tectonic deformation in the Himalayan orogen [e.g., *Beaumont et al*., 2001; *Thiede et al*., 2004; *Hodges et al*., 2004]. In our study area, we also observe bands of high annual rainfall near the MBT and at the transition from the LH to the HH, similar to other parts of the Himalaya [*Bookhagen and Burbank*, 2006]. But our results suggest that observed spatial variations in mean annual rainfall (based on TRMM data) do not influence ^{10}Be-derived tributary erosion rates ($R^2 \leq 0.0001$ for linear or power law fit). Specifically, the tributaries which are closest to the outer rainfall band near the MBT (#1, #2, #9) have erosion rates below 0.6 mm yr^{-1}, despite annual rainfall amounts that are similar or greater than in the HH (Table 3). Therefore, precipitation peaks in the Yamuna catchment are found where mean surface elevations change dramatically (Figures 1 and 2), but they do not coincide with peaks in erosion or topographic steepness. It should be noted, however, that these observations are only valid across the range of rather high annual rainfall amounts in the Yamuna catchment and should not be extrapolated to more arid environments.

6.4. Transient Versus Steady State Landscapes

[46] In the framework of the stream-power model, graded channel profiles that can be described with a single channel steepness index are commonly interpreted to be in steady state with external forcing factors, that is, with climate, lithology, and rock uplift [e.g., *Wobus et al*., 2006; *Kirby and Whipple*, 2012]. We noticed that our studied catchments often show larger variability of k_{sn} values compared to what has been observed in other areas [e.g., *Ouimet et al*., 2009; *DiBiase et al*., 2010]. While part of this scatter may be attributed to the larger catchment sizes in our study and associated spatial variations in climate, lithology, and rock uplift, we also observed some suspiciously systematic deviations from graded channel profiles. For instance, a number of tributaries appear to have unusually gentle channels close to their headwaters, particularly in the lower Tons Valley (e.g., #10 in Figure 3), which may point to partial preservation of a relict landscape. Although gently sloping headwater areas are known from glaciated catchments [*Brocklehurst and Whipple*, 2004], this explanation is unlikely where peak elevations are below 3000 m and where no other

Figure 11. Field photograph of the headwaters in tributary #4. Arrow indicates position of channel and flow direction. View is to the SE.

signs for glaciation exist. Furthermore, several tributary channels in the lower Tons Valley, the Pabbar River itself, and tributary #4 in the Yamuna Valley display knickzones before they join the trunk rivers (note that our samples from any of these tributaries stem from above the knickzones). In the case of tributary #16, for example, the knickzone appears to represent an epigenetic gorge [e.g., *Ouimet et al*., 2008], probably related to an episode of valley aggradation and incision. But this mechanism cannot explain all observed knickzones.

[47] A particularly pronounced knickzone exists where tributary #4, which covers a significant portion of the interfluve between the Yamuna and Tons valleys, joins the Yamuna River (Figures 3 and 6). This tributary was already identified as having an anomalously low channel gradient, which is almost identical to that of the Yamuna River at equal distances from their confluence, although its upstream area is less than a third compared to the Yamuna River. Because its valley is rather narrow in the lower part of the catchment and is getting progressively wider and alluvium-covered farther up (Figure 11), the downstream gradient of the bedrock below the fill may be even lower. Furthermore, this tributary lies in the center of an area (cf., neighboring tributaries #4, #5, #11) that is characterized by low ^{10}Be-derived erosion rates, local relief, k_{sn}, and ω (Figures 5 and 6). An explanation may be that this tributary drains the remnant of a once larger catchment whose headwaters have been captured by the Tons River. Such hypothesis is supported by the ridgeline topography of this tributary (Figure 12), which has a peculiar low elevation where it borders the adjacent catchments in the Tons Valley (tributary #11 and the one north of it). A stream capture event in the upper Tons Valley would have abruptly increased the discharge of the Tons River, forcing it to lower its gradient, which may explain the knickzones in the lower reaches of the Pabbar and several tributary channels in the lower Tons Valley. Concurrently, channel incision of tributary #4 would have slowed down, producing a knickpoint at the confluence with the Yamuna River. We emphasize that these ideas are speculative in nature and additional field evidence is needed to shed more light on this peculiar feature.

[48] Although we see ample evidence in the landscape that defies a steady state assumption and although some channels have clearly been shaped by glaciers in the past (#13–15) and others may still be affected by mass-wasting deposits in some reaches (#1), most of the analyzed channels appear as fairly straight lines in the χ plots (Figure 5), suggesting their morphologies are not far from steady state [*Perron and Royden*, 2012]. Moreover, a correlation between ^{10}Be-derived erosion rates and k_{sn} is expected for landscapes that are in steady state with external forcing factors [*Snyder et al*., 2003; *Kirby and Whipple*, 2012]. Because the above identified areas with evidence for landscape disequilibrium are either relatively small in extent or downstream from our sampling locations, we argue that they do not affect the ^{10}Be data and the catchment-averaged parameters much and that the present landscape in most of the nonglaciated tributary catchments is reasonably close to steady state. Furthermore, similar ^{10}Be-derived erosion rates and k_{sn} values for studied catchments in the LH and HH let us conclude that differences in rock erodibility have, like climatic variations, a minor effect on erosion rates and channel steepness in our study area.

6.5. Tectonic Influence on the Spatial Distribution of Erosion

[49] Published shortening rates and geophysical data [*Powers et al*., 1998; *Caldwell et al*., 2013] on the subsurface structure of the Garhwal Himalaya allow us to compare our results with a first-order assessment of expected rock uplift rates. GPS-based arc-normal horizontal shortening rates in the Garhwal Himalaya have been reported to be 13.6 ± 5.5 mm yr^{-1} and similar to shortening rates in eastern Nepal [*Styron et al*., 2011]. More recent modeling of a larger geodetic data set suggests shortening rates of ~18–20 mm yr^{-1} in Nepal [*Ader et al*., 2012], consistent with Holocene shortening rates [*Lavé and Avouac*, 2000], which most likely implies similar shortening rates in Garhwal. If we neglect any internal deformation and assume that the Himalayan orogenic wedge is sliding with an average rate of ~14–20 mm yr^{-1} over the midcrustal ramp in the MHT [*Caldwell et al*., 2013], we would expect maximum rock uplift rates of ~4.0–5.7 mm yr^{-1} (Figure 13). This range of uplift rates is clearly higher than most of our erosion rates from the HH. However, we note that the erosion rate from

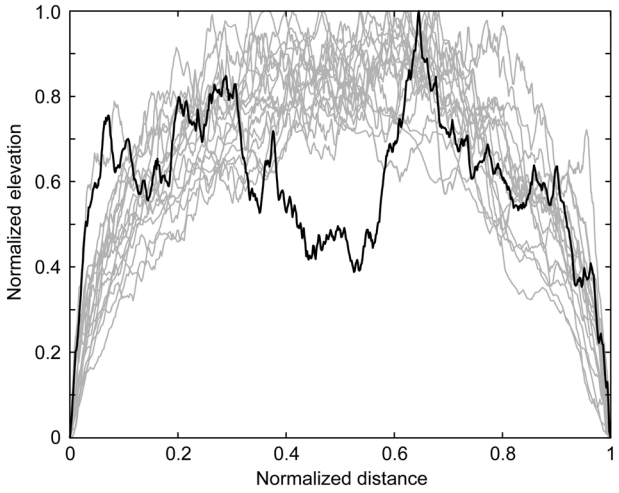

Figure 12. Normalized elevations of ridgelines of the studied tributary catchments. Black line denotes tributary #4 with a pronounced low where most other catchments reach their highest elevations.

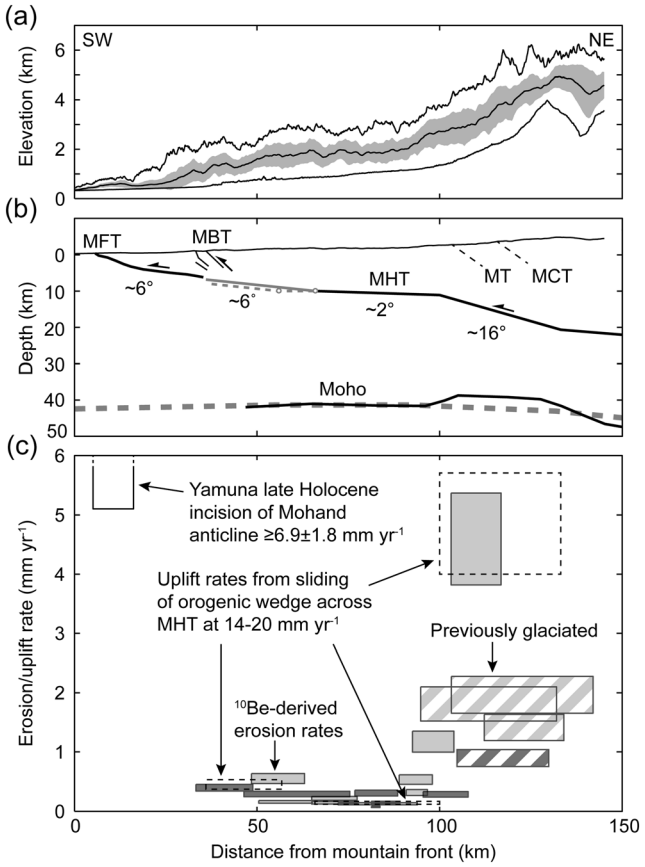

Figure 13. Uplift and erosion across the Yamuna catchment. (a) Surface elevations along 50 km wide swath profile (cf., Figures 1 and 2). (b) Depth of Main Himalayan Thrust fault (MHT) based on seismic reflection profiles between MFT and MBT in the Dehra Dun Valley [*Powers et al*., 1998] and at distances >70 km from the mountain front based on teleseismic receiver-function studies along the Alaknanda River, approximately 100 km farther southeast [*Caldwell et al*., 2013]. Gray lines denote possible depth of MHT, with inflection point at 30 km (20 km) distance from surface trace of MBT. See text for details. Depth of Moho is based on teleseismic receiver-function studies (black) and calculated deflection for a flexed beam (dashed) [*Caldwell et al*., 2013]. (c) Erosion rate estimates (solid rectangles) and expected uplift rates (dashed rectangles) for rigid-sliding model across MHT. Catchment-averaged tributary ^{10}Be-erosion rates have been projected into swath profile. Width of rectangle indicates lateral extent of catchment. Dark gray rectangles denote catchments lying northwest, outside of swath profile. Hatched rectangles denote catchments that currently are or have previously been partly glaciated. Incision rate into Mohand anticline is based on Holocene strath terrace [*Wesnousky et al*., 1999].

tributary #8 falls within this range and that the other, more slowly eroding tributaries, have been or still are ice covered to at least some degree. Thus, if glacial incision rates during the Pleistocene were higher than present-day erosion rates, it may well be that in the long-term, these catchments are eroding at higher average rates that are closer to the erosion rate of tributary #8.

[50] It has been shown that ~75% of the shortening in central Nepal occurs by underthrusting of India beneath the Himalaya and Tibet and only ~25% by overthrusting [*Avouac*, 2003; *Bollinger et al*., 2004]. Assuming a similar ratio in Garhwal, we obtain an overthrusting rate of ~3.5–5 mm yr^{-1}, which would result in a rock uplift rate of ~0.12–0.17 mm yr^{-1} above the 2° dipping flat in the MHT (Figure 13). This range is close to our measured values in the southeastern part of the Yamuna catchment (~0.1–0.2 mm yr^{-1}), with the notable exception of tributary #1 (0.55 ± 0.04 mm yr^{-1}). In the northwestern part, however, where the topography is comparatively higher and dominated by the HHS, erosion rates appear to be systematically higher too (~0.3 mm yr^{-1}; dark gray rectangles in Figure 13c), possibly pointing at lateral variations in the geometry of the MHT.

[51] Farther southwest, the continuation of the MHT is less certain, but it has to connect from its ~10 km depth under the LH to a depth of ~4–5 km beneath the Dehra Dun Valley [*Powers et al*., 1998]. Our ^{10}Be data indicate a slight increase in erosion rates toward the MBT that could be due to higher uplift rates above a steeper MHT. Alternatively, more recent activity on the MBT and proximal faults could also account for this increase and appears to be supported by tightly folded Sub-Himalayan sediments in the adjacent Santaurgarh anticline, surface-breaking faults, and uplifted alluvial-fan deposits [*Thakur et al*., 2007]. In any case, magnetostratigraphic dating of Siwalik-group sediments in the Dehra Dun Valley to <0.78 Ma [*Kumar et al*., 2003] and a reconstructed total shortening of only 5 km across the Mohand anticline [*Powers et al*., 1998] document rather recent initiation of the MFT and uplift of the Mohand anticline [*Barnes et al*., 2011]. This implies that the MBT and related nearby faults have accommodated most of the frontal shortening in the recent geologic past (<2 Ma), which could explain the higher erosion rates and channel steepness compared to areas farther northeast (Figure 6).

[52] If we assume that catchments in the LH are laterally advected across the MHT from a gently dipping portion (~2°) into a region of steeper dip, the landscape would have to adjust to the higher uplift rates, likely by knickpoints passing through the drainage network [e.g., *Whipple and Tucker*, 1999; *Harkins et al*., 2007; *Schildgen et al*., 2012]. Pronounced knickpoints in the lowest Yamuna tributaries, separating a lower-relief upper part of the catchment (>1100 m) from a higher-relief lower part of the catchment, could indeed be related to such an adjustment (Figure 6). The k_{sn} values ($\theta_{ref} = 0.45$) derived by the integral method for the upper and lower parts of the catchment that joins the Yamuna near the MBT (Figure 6) are $\sim 96 \pm 2$ and 192 ± 5 m$^{0.9}$, respectively, which would correspond to erosion rates of ~0.01–0.09 and ~0.44–0.51 mm yr^{-1}, based on the nonlinear relationships (Figures 7c and 8). The lower erosion rate estimate compares well with our expected rock uplift rates associated with the gentle (~2°) dipping part of the MHT. The higher erosion rate estimate is similar to a rock uplift rate of 0.37–0.53 mm yr^{-1} that would result from overthrusting a ~6° dipping MHT, as suggested by seismic reflection profiles beneath the Dehra Dun Valley [*Powers et al*., 1998].

[53] We estimated the relative incision (Δz) since knickpoint initiation, by projecting the low-k_{sn} upper channel of the tributary toward the outlet [cf., *Harkins et al*., 2007; *Schildgen et al*., 2012], to be on the order of $\sim 440 \pm 11$ m (Figure 14a). The Δz is proportional to the difference in uplift

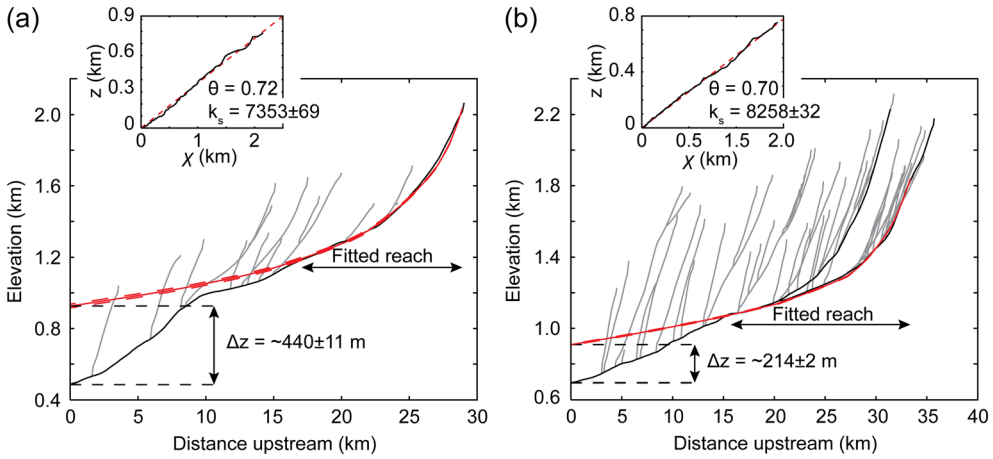

Figure 14. Drainage networks of the lowermost tributaries to the Yamuna River, located (a) just upstream of the MBT and (b) approximately 20 km upstream from the Main Boundary Thrust. Inset figures show χ plot of fitted trunk stream reaches in the upper part of the catchment. Best fit concavity (θ) and channel steepness indices (k_s) are used to reconstruct channel elevations, shown in red below. The Δz gives elevation difference at outlet between present channel and reconstructed channel. See Figure 6 for location of drainages.

rates before (u_1) and after (u_2) a sudden increase in uplift and the time elapsed since the change in uplift, according to $\Delta z = \Delta t(u_2 - u_1)$ [*Whipple and Tucker*, 1999]. For the above mentioned uplift rates associated with a 2° and 6° dipping MHT and an overthrusting rate of 3.5–5 mm yr^{-1}, the change in uplift rate would have occurred at ~1.3–1.8 Ma. For a shortening rate of ~14–20 mm yr^{-1}, the change in the dip of the MHT would thus be located at a distance of ~18–36 km from the MBT. Performing the same analysis for another tributary of the Yamuna that is located ~10 km farther northeast along the profile in Figure 13 and which has a similar channel steepness in its upper part ($k_{sn} = 97 \pm 2$ m$^{0.9}$; $\theta_{ref} = 0.45$) but is less steep ($k_{sn} = 144 \pm 2$ m$^{0.9}$) in its lower part yields a change in uplift rate at ~0.6–0.9 Ma, for a reconstructed Δz of ~214 ± 2 m (Figure 14b) and the same uplift rates as before. Taking the greater distance of this tributary from the MBT into account, this would correspond to a change in dip of the MHT at a distance of ~18–28 km from the MBT.

[54] We note that the two tributaries have different orientations with respect to the regional structural grain, which would have affected the timing at which certain parts of the catchment experienced a change in uplift. Although the outlets of both catchments are near or at the leading edge of the catchment with respect to their advection direction, if knickpoint retreat occurs faster than horizontal advection (at the shortening rate of ~14–20 mm yr^{-1}), the calculated timing of change in uplift rate is likely to be underestimated. Because the horizontal distance of knickpoint retreat in the shortening direction is ~10 km for the lower, more perpendicular-oriented tributary, which is much less than the ~18–36 km of transport across a steeper segment in the MHT, we doubt that this complicating fact introduces significant errors to our calculation.

[55] For a distance of 30 km, the increase in dip would occur just at the southwestern end of where the MHT geometry appears reasonably well imaged by geophysical data [*Caldwell et al.*, 2013] and make the MHT almost line up with its depth underneath the Dehra Dun Valley (Figure 13). At shorter distances, the MHT would have to involve another steep section beneath the MBT, which has also been considered by *Powers et al.* [1998]. In any case, a scenario in which the gently dipping part of the MHT attains a steeper gradient of ~6° at a distance of ~60–70 km from the MFT is consistent with an increase in ^{10}Be-derived tributary erosion rates and the preservation of relict landscapes in the lowermost tributaries of the Yamuna upstream of the MBT.

7. Conclusions

[56] We have presented 25 new ^{10}Be-derived catchment-averaged erosion rates across the Garhwal Himalaya, northern India. Erosion rates appear to be largely free of systematic biases in most of the study area, but the samples from the steep and more rapidly eroding High Himalaya are subject to greater geomorphic uncertainties due to potentially important infrequent and deep-seated landslides, ubiquitous rock falls and debris flows, and past glacial sculpting of the landscape. The tributary erosion-rate data correlate well with catchment-averaged values of 5 km radius local relief, normalized channel steepness indices, and specific stream power but to varying degrees of nonlinearity. The limited number of samples from the High Himalaya does not yet allow accurately defining these relationships at high-erosion rates, but high and similar explanatory power of the tested parameters suggests that climatic differences that result in twofold to threefold differences in annual runoff do not significantly affect erosion rates. There are also no discernible differences in erosion rates that could be related to lithological variations between the Lesser Himalaya (LH) and High Himalaya (HH). Analysis of our results from larger main stem rivers indicates significant deviations of ^{10}Be-derived erosion rates from predicted erosion rates based on morphometric parameters, which may be related to nonproportional sediment supply from different tributaries and lack of mixing in main stem channels.

[57] The spatial variations of erosion across the Yamuna catchment are well explained with a tectonic model that relates differences in rock uplift rates to differences in the dip angle of the Main Himalayan Thrust fault (MHT) and assuming the landscape is not far from steady state. The magnitude of erosion in the LH compares well with rock uplift rates expected from a gentle (2°) dipping MHT, as constrained by

geophysical data, and an overthrusting rate that is ~25% of the shortening rate (~14–20 mm yr^{-1}). Slightly increasing erosion rates toward the MBT point at a steeper angle of the MHT; this appears to be supported by knickpoints in tributaries of the Yamuna near the MBT. Expected rock uplift rates in the HH are higher than most of the ^{10}Be-derived erosion rates but may be reconciled with a glacial overprint during the Pleistocene, suggesting that interglacial erosion rates in the HH may be significantly lower than during glacial times.

[58] **Acknowledgments.** This research was funded by the DFG graduate school GK1364 (DFG grant STR373/21-1). D.S. is grateful for support by the Alexander von Humboldt Foundation. We thank J.-P. Avouac for helpful discussions and T. Tsering Lonpo for support during fieldwork. The constructive comments of A. Webb and two anonymous reviewers, and the associate editor N. Gasparini helped improving the manuscript.

References

Ader, T., et al. (2012), Convergence rate across the Nepal Himalaya and interseismic coupling on the Main Himalayan Thrust: Implications for seismic hazard, *J. Geophys. Res.*, *117*, B04403. doi:10.1029/2011JB009071.

Ahmad, T., N. Harris, M. J. Bickle, H. J. Chapman, J. Bunbury, and C. Prince (2000), Isotopic constraints on the structural relationships between the Lesser Himalayan Series and the High Himalayan Crystalline Series, Garhwal Himalaya, *Geol. Soc. Am. Bull.*, *112*, 467–477.

Ahnert, F. (1970), Functional relationships between denudation, relief, and uplift in large mid-latitude basins, *Am. J. Sci.*, *268*, 243–263.

Andermann, C., A. Crave, R. Gloaguen, P. Davy, and S. Bonnet (2012), Connecting source and transport: Suspended sediments in the Nepal Himalayas, *Earth Planet. Sci. Lett.*, *351-352*, 158–170, doi:10.1016/j.epsl.2012.06.059.

Arendt, A., et al. (2012), *Randolph Glacier Inventory [v2.0]: A Dataset of Global Glacier Outlines, Global Land Ice Measurements from Space*, Digital Media, Boulder Colorado, USA.

Avouac, J.-P. (2003), Mountain building, erosion, and the seismic cycle in the Nepal Himalaya, *Adv. Geophys.*, *46*, 1–80, doi:10.1016/S0065-2687(03)46001-9.

Bagnold, R. A. (1977), Bed load transport by natural rivers, *Water Resour. Res.*, *13*, 303–312, doi:10.1029/WR013i002p00303.

Balco, G., J. Stone, N. Lifton, and T. Dunai (2008), A complete and easily accessible means of calculating surface exposure ages or erosion rates from ^{10}Be and ^{26}Al measurements, *Quat. Geochronol.*, *3*, 174–195, doi:10.1016/j.quageo.2007.12.001.

Barnad, P. L., L. A. Owen, M. C. Sharma, and R. C. Finkel (2001), Natural and human-induced landsliding in the Garhwal Himalaya of northern India, *Geomorphology*, *40*, 21–35.

Barnes, J. B., Densmore, A. L., Mukul, M., Sinha, R., Jain, V., and S. K. Tandon (2011), Interplay between faulting and base level in the development of Himalayan frontal fold topography, *J. Geophys. Res.*, *116*, F03012, doi:10.1029/2010JF001841.

Beaumont, C., R. A. Jamieson, M. H. Nguyen, and B. Lee (2001), Himalayan tectonics explained by extrusion of a low-viscosity crustal channel coupled to focused surface denudation, *Nature*, *414*, 738–742, doi:10.1038/414738a.

Bierman, P., and E. J. Stieg (1996), Estimating rates of denudation using cosmogenic isotope abundances in sediment, *Earth Surf. Proc. Land.*, *21*, 125–139.

Binnie, S. A., W. M. Phillips, M. A. Summerfield, and L. K. Fifield (2006), Sediment mixing and basin-wide cosmogenic nuclide analysis in rapidly eroding mountainous environments, *Quatern. Geochron.*, *1*, 4–14, doi:10.1016/j.quageo.2006.06.013.

Bollinger, L., J.-P. Avouac, O. Beyssac, E. J. Catlos, T. M. Harrison, M. Grove, B. Goffe, and S. Sapkota (2004), Thermal structure and exhumation history of the Lesser Himalaya in central Nepal, *Tectonics*, *23*, TC5015, doi:10.1029/2003TC001564.

Bookhagen, B., and D. W. Burbank (2006), Topography, relief, and TRMM-derived rainfall variations along the Himalaya, *Geophys. Res. Lett.*, *33*, L08405, doi:10.1029/2006GL026037.

Bookhagen, B., and D. W. Burbank (2010), Toward a complete Himalayan hydrologic budget: Spatiotemporal distribution of snowmelt and rainfall and their impact on river discharge, *J. Geophys. Res.*, *115*, F03019, doi:10.1029/2009JF001426.

Bookhagen, B., and M. R. Strecker (2012), Spatiotemporal trends in erosion rates across a pronounced rainfall gradient: Examples from the southern Central Andes, *Earth Planet. Sci. Lett.*, *327-328*, 97–110, doi:10.1016/j.epsl.2012.02.005.

Bookhagen, B., R. C. Thiede, and M. R. Strecker (2005), Late Quaternary intensified monsoon phases control landscape evolution in the northwest Himalaya, *Geology*, *33*, 149–152.

Bookhagen, B., D. Fleitmann, K. Nishiizumi, M. R. Strecker, and R. Thiede (2006), Holocene monsoonal dynamics and fluvial terrace formation in the northwest Himalaya, India, *Geology*, *34*(7), 601–604, doi:10.1130/G22698.1.

Brocklehurst, S. H., and K. X. Whipple (2004), Hypsometry of glaciated landscapes, *Earth Surf. Proc. Land.*, *29*, 907–926, doi:10.1002/esp.1083.

Brown, E. T., R. F. Stallard, M. C. Larsen, and G. M. Raisbeck (1995), Denudation rates determined from the accumulation of in situ-produced ^{10}Be in the Luquillo Experimental Forest, Puerto Rico, *Earth Planet. Sci. Lett.*, *129*, 193–202.

Burbank, D. W., J. Leland, E. Fielding, R. S. Anderson, N. Brozovic, M. R. Reid, and C. Duncan (1996), Bedrock incision, rock uplift and threshold hillslopes in the northwestern Himalayas, *Nature*, *379*, 505–510.

Burbank, D. W., A. E. Blythe, J. Putkonen, B. Pratt-Sitaula, E. Gabet, M. Oskin, A. Barros, and T. P. Ojha (2003), Decoupling of erosion and precipitation in the Himalayas, *Nature*, *426*, 652–655, doi:10.1038/nature02187.

Caldwell, W. B., S. L. Klemperer, J. F. Lawrence, S. S. Rai, and Ashish (2013), Characterizing the Main Himalayan Thrust in the Garhwal Himalaya, India with receiver function CCP stacking, *Earth Planet. Sci. Lett.*, *367*, 15–27, doi:10.1016/j.epsl.2013.02.009.

Cattin, R., and J. P. Avouac (2000), Modeling mountain building and the seismic cycle in the Himalaya of Nepal, *J. Geophys. Res.*, *105*, 13,389–13,407, doi:10.1029/2000JB900032.

Cerling, T. E., and H. Craig (1994), Cosmogenic production rates of ^{3}He from 39 to 46°N latitude, western USA and France, *Geochim. Cosmochim. Acta*, *58*, 249–255.

Chmeleff, J., F. von Blanckenburg, K. Kossert, and D. Jakob (2010), Determination of the ^{10}Be half-life by multicollector ICP-MS and liquid scintillation counting, *Nucl. Instr. Meth. Res. B*, *268*, 192–199.

Clift, P. D., K. V. Hodges, D. Heslop, R. Hannigan, H. V. Long, and G. Calves (2008), Correlation of Himalayan exhumation rates and Asian monsoon intensity, *Nat. Geosci.*, *1*, 875–880, doi:10.1038/ngeo351.

Cyr, A. J., D. E. Granger, V. Olivetti, and P. Molin (2010), Quantifying rock uplift rates using channel steepness and cosmogenic nuclide-determined erosion rates: Examples from northern and southern Italy, *Lithosphere*, *2*(3), 188–198, doi:10.1130/L96.1.

Dalai, T. K., S. Krishnaswami, and M. M. Sarin (2002), Major ion chemistry in the headwaters of the Yamuna river system: Chemical weathering, its temperature dependence and CO_2 consumption in the Himalaya, *Geochim. Cosmochim. Acta*, *66*, 3397–3416.

DiBiase, R. A., and K. X. Whipple (2011), The influence of erosion thresholds and runoff variability on the relationships among topography, climate, and erosion rate, *J. Geophys. Res.*, *116*, F04036, doi:10.1029/2011JF002095.

DiBiase, R. A., K. X. Whipple, A. M. Heimsath, and W. B. Ouimet (2010), Landscape form and millennial erosion rates in the San Gabriel Mountains, CA, *Earth Planet. Sci. Lett.*, *289*(1-2), 134–144, doi:10.1016/j.epsl.2009.10.036.

Dunne, J., D. Elmore, and P. Muzikar (1999), Scaling factors for the rates of production of cosmogenic nuclides for geometric shielding and attenuation at depth on sloped surfaces, *Geomorphology*, *27*, 3–11.

Finnegan, N. J., G. Roe, D. R. Montgomery, and B. Hallet (2005), Controls on the channel width of rivers: Implications for modeling fluvial incision of bedrock, *Geology*, *33*, 229–232, doi:10.1130/G21171.1.

Fisher, G. B., B. Bookhagen, and C. B. Amos (2013), Channel planform geometry and slopes from freely available high-spatial resolution imagery and DEM fusion: Implications for channel width scalings, erosion proxies, and fluvial signatures in tectonically active landscapes, *Geomorphology*, doi:10.1016/j.geomorph.2013.04.011.

Flint, J. J. (1974), Stream gradient as a function of order, magnitude, and discharge, *Water Resour. Res.*, *10*, 969–973.

France-Lanord, C., and L. A. Derry (1997), Organic carbon burial forcing of the carbon cycle from Himalayan erosion, *Nature*, *390*, 65–66, doi:10.1038/36324.

France-Lanord, C., M. Evans, J.-E. Hurtrez, and J. Riotte (2003), Annual dissolved fluxes from Central Nepal rivers: Budget of chemical erosion in the Himalayas, *C. R. Geosci.*, *335*, 1131–1140.

Gabet, E., D. W. Burbank, J. K. Putkonen, B. A. Pratt-Sitaula, and T. Ojha (2004), Rainfall thresholds for landsliding in the Himalayas of Nepal, *Geomorphology*, *63*, 131–143, doi:10.1016/j.geomorph.2004.03.011.

Gabet, E. J., D. W. Burbank, B. Pratt-Sitaula, J. Putkonen, and B. Bookhagen (2008), Modern erosion rates in the High Himalayas of

Nepal, *Earth Planet. Sci. Lett.*, *267*(3–4), 482–494, doi:10.1016/j.epsl.2007.11.059.

Galy, A., and C. France-Lanord (2001), Higher erosion rates in the Himalaya: Geochemical constraints on riverine fluxes, *Geology*, *29*, 23–26.

Galy, V., C. France-Lanord, O. Beyssac, P. Faure, H. Kudrass, and F. Palhol (2007), Efficient organic carbon burial in the Bengal fan sustained by the Himalayan erosional system, *Nature*, *450*, 407–410.

Gansser, A. (1964), *Geology of the Himalayas*, pp. 289, Interscience, London.

Garzanti, E., G. Vezzoli, S. Ando, J. Lave, M. Attal, C. France-Lanord, and P. DeCelles (2007), Quantifying sand provenance and erosion (Marsyandi River, Nepal Himalaya), *Earth Planet. Sci. Lett.*, *258*, 500–515, doi:10.1016/j.epsl.2007.04.010.

Godard, V., R. Cattin, and J. Lavé (2004), Numerical modeling of mountain building: Interplay between erosion law and crustal rheology, *Geophys. Res. Lett.*, *31*, L23607, doi:10.1029/2004GL021006.

Godard, V., D. W. Burbank, D. L. Bourlès, B. Bookhagen, R. Braucher, and G. B. Fisher (2012), Impact of glacial erosion on ^{10}Be concentrations in fluvial sediments of the Marsyandi catchment, central Nepal, *J. Geophys. Res.*, *117*, F03013, doi:10.1029/2011JF002230.

Granger, D. E., J. W. Kirchner, and R. Finkel (1996), Spatially averaged long-term erosion rates measured from in situ-produced cosmogenic nuclides in alluvial sediment, *J. Geol.*, *104*, 249–257.

Hack, J. T. (1957), Studies of longitudinal stream profiles in Virginia and Maryland, *U. S. Geol. Survey Prof. Papers*, 294-B, p. 97.

Harkins, N., E. Kirby, A. Heimsath, R. Robinson, and U. Reiser (2007), Transient fluvial incision in the headwaters of the Yellow River, northeastern Tibet, China, *J. Geophys. Res.*, *112*, F03S04, doi:10.1029/2006JF000570.

Herman, F., et al. (2010), Exhumation, crustal deformation, and thermal structure of the Nepal Himalaya derived from the inversion of thermochronological and thermobarometric data and modeling of the topography, *J. Geophys. Res.*, *115*, B06407, doi:10.1029/2008JB006126.

Hodges, K. V., C. Wobus, K. Ruhl, T. Schildgen, and K. Whipple (2004), Quaternary deformation, river steepening, and heavy precipitation at the front of the Higher Himalayan ranges, *Earth Planet. Sci. Lett.*, *220*, 379–389, doi:10.1016/S0012-821X(04)00063-9.

Howard, A. D., and G. Kerby (1983), Channel changes in badlands, *Geol. Soc. Am. Bull.*, *94*(6), 739–752, doi:10.1130/0016-7606(1983)94<739:CCIB>2.0.CO;2.

Huffman, G. J., R. F. Adler, D. T. Bolvin, G. Gu, E. J. Nelkin, K. P. Bowman, Y. Hong, E. F. Stocker, and D. B. Wolff (2007), The TRMM Multi-satellite Precipitation Analysis: Quasi-Global, Multi-Year, Combined-Sensor Precipitation Estimates at Fine Scales, *J. Hydrometeor.*, *8*, 38–55.

Hurtez, J.-E., F. Lucazeau, J. Lave, and J.-P. Avouac (1999), Investigation of the relationships between basin morphology, tectonic uplift, and denudation from the study of an active fold belt in the Siwalik Hills, central Nepal, *J. Geophys. Res.*, *104*, 12,779–12,796.

Jha, P. K., V. Subramanian, and R. Sitasawad (1988), Chemical and sediment mass transfer in the Yamuna River—A tributary of the Ganges system, *J. Hydrol.*, *104*, 237–246.

Kirby, E., and K. X. Whipple (2012), Expression of active tectonics in erosional landscapes, *J. Struct. Geol.*, *44*, 54–75.

Kirchner, J. W., R. C. Finkel, C. S. Riebe, D. E. Granger, J. L. Clayton, J. G. King, and W. F. Megahan (2001), Mountain erosion over 10 yr, 10 k.y., and 10 m.y. time scales, *Geology*, *29*, 591–594.

Kohl, C. P., and K. Nishiizumi (1992), Chemical isolation of quartz for measurement of in-situ-produced cosmogenic nuclides, *Geochim. Cosmochim. Acta*, *56*, 3583–3587.

Koons, P. O. (1990), Two-sided orogen: Collision and erosion from the sandbox to the Southern Alps, New Zealand, *Geology*, *18*, 679–682.

Korschinek, G., et al. (2010), A new value for the half-life of ^{10}Be by Heavy-Ion Elastic Recoil Detection and liquid scintillation counting, *Nucl. Instr. Meth. Res. B*, *268*, 187–191.

Kumar, R., S. K. Ghosh, R. K. Mazari, and S. J. Sagode (2003), Tectonic impact on the fluvial deposits of Plio-Pleistocene Himalayan foreland basin, India, *Sediment. Geol.*, *158*, 209–234, doi:10.1016/S0037-0738(02)00267-1.

Lague, D., and P. Davy (2003), Constraints on the long-term colluvial erosion law by analyzing slope-area relationships at various tectonic uplift rates in the Siwaliks Hills (Nepal), *J. Geophys. Res.*, *108*, 2129, doi:10.1029/2002JB001893.

Lague, D., N. Hovius, and P. Davy (2005), Discharge, discharge variability, and the bedrock channel profile, *J. Geophys. Res.*, *110*, F04006, doi:10.1029/2004JF000259.

Lal, D. (1991), Cosmic ray labeling of erosion surfaces: In situ nuclide production rates and erosion models, *Earth Planet. Sci. Lett.*, *104*(2–4), 424–439.

Lavé, J., and J.-P. Avouac (2000), Active folding of fluvial terraces across the Siwaliks Hills, Himalayas of central Nepal, *J. Geophys. Res.*, *105*, 5735–5770.

Lavé, J., and J.-P. Avouac (2001), Fluvial incision and tectonic uplift across the Himalayas of central Nepal, *J. Geophys. Res.*, *106*, 26,561–26,591.

Lupker, M., P.-H. Blard, J. Lavé, C. France-Lanord, L. Leanni, N. Puchol, J. Charreau, and D. Bourlès (2012), ^{10}Be-derived Himalayan denudation rates and sediment budgets in the Ganga basin, *Earth Planet. Sci. Lett.*, *333-334*, 146-156, doi:10.1016/j.epsl.2012.04.020.

Masek, J. G., B. L. Isacks, T. L. Gubbels, and E. J. Fielding (1994), Erosion and tectonics at the margins of continental plateaus, *J. Geophys. Res.*, *99*, 13,941–13,956.

Milliman, J. D., and J. D. M. Syvitski (1992), Geomorphic/tectonic control of sediment discharge to the ocean: The importance of small mountainous rivers, *J. Geol.*, *100*, 525–544.

Montgomery, D. R., and M. T. Brandon (2002), Topographic controls on erosion rates in tectonically active mountain ranges, *Earth Planet. Sci. Lett.*, *201*, 481–489.

Montgomery, D. R., and K. B. Gran (2001), Downstream variations in the width of bedrock channels, *Water Resour. Res.*, *37*(6), 1841–1846, doi:10.1029/2000WR900393.

Montgomery, D. R., and D. B. Stolar (2006), Reconsidering Himalayan river anticlines, *Geomorphology*, *82*, 4–15.

Niemi, N., M. Oskin, D. Burbank, A. Heimsath, and E. Gabet (2005), Effects of bedrock landslides on cosmogenically determined erosion rates, *Earth Planet. Sci. Lett.*, *237*, 480–498, doi:10.1016/j.epsl.2005.07.009.

Nishiizumi, K., M. Imamura, M. W. Caffee, J. R. Southon, R. C. Finkel, and J. McAninch (2007), Absolute calibration of ^{10}Be AMS standards, *Nucl. Instr. Meth. Res. B*, *258*, 403–413.

Norton, K. P., F. von Blanckenburg, and P. W. Kubik (2011), Cosmogenic nuclide-derived rates of diffusive and episodic erosion in the glacially sculpted upper Rhone Valley, Swiss Alps, *Earth Surf. Proc. Land.*, *35*, 651–662, doi:10.1002/esp.1961.

Ouimet, W. B., K. X. Whipple, B. T. Crosby, J. P. Johnson, and T. F. Schildgen (2008), Epigenetic gorges in fluvial landscapes, *Earth Surf. Proc. Land.*, *33*, 1993–2009, doi:10.1002/esp.1650.

Ouimet, W. B., K. X. Whipple, and D. E. Granger (2009), Beyond threshold hillslopes: Channel adjustment to base-level fall in tectonically active mountain ranges, *Geology*, *37*(7), 579–582, doi:10.1130/G30013A.1.

Owen, L. A., U. Kamp, G. A. Khattak, E. L. Harp, D. K. Keefer, and M. A. Bauer (2008), Landslides triggered by the 8 October 2005 Kashmir earthquake, *Geomorphology*, *94*, 1–9.

Perron, J. T., and L. Royden (2012), An integral approach to bedrock river profile analysis, *Earth Surf. Proc. Land.*, *38*, 570–576, doi:10.1002/esp.3302.

Pinet, P., and M. Souriau (1988), Continental erosion and large-scale relief, *Tectonics*, *7*, 563–582.

Powers, P. M., R. J. Lillie, and R. S. Yeats (1998), Structure and shortening of the Kangra and Dehra Dun reentrants, Sub-Himalaya, India, *Geol. Soc. Am. Bull.*, *110*, 1010–1027, doi:10.1130/0016-7606(1998)110<1010:SASOTK>2.3.CO;2.

Pratt, B., D. W. Burbank, A. Heimsath, and T. Ojha (2002), Impulsive alluviation during early Holocene strengthened monsoons, central Nepal Himalaya, *Geology*, *30*, 911–914, doi:10.1130/0091-7613(2002)030<0911:IADEHS>2.0.CO;2.

Pratt-Sitaula, B., M. Garde, D. W. Burbank, M. Oskin, A. Heimsath, and E. Gabet (2007), Bedload-to-suspended load ratio and rapid bedrock incision from Himalayan landslide-dam lake record, *Quatern. Res.*, *68*, 111–120.

Rahaman, W., S. K. Singh, R. Sinha, and S. K. Tandon (2009), Climate control on erosion distribution over the Himalaya during the past ~100 ka, *Geology*, *37*, 559–562, doi:10.1130/G25425A.1.

Rao, K. L. (1975), *India's Water Wealth*, pp. 255, Orient Longman Ltd., New Delhi.

Raymo, M. E., and W. F. Ruddiman (1992), Tectonic forcing of late Cenozoic climate, *Nature*, *359*, 117–122.

Riebe, C. S., and D. E. Granger (2013), Quantifying effects of deep and near-surface chemical erosion on cosmogenic nuclides in soils, saprolite, and sediment, *Earth Surf. Proc. Land.*, *38*, 523–533, doi:10.1002/esp.3339.

Roe, G. H. (2005), Orographic precipitation, *Annu. Rev. Earth Planet. Sci.*, *33*, 645–671, doi:10.1146/annurev.earth.33.092203.122541.

Scherler, D., B. Bookhagen, M. R. Strecker, F. von Blanckenburg, and D. Rood (2010), Timing and extent of late Quaternary glaciation in the western Himalaya constrained by ^{10}Be moraine dating in Garhwal, India, *Quater. Sci. Rev.*, *29*, 815–831.

Schildgen, T. F., W. M. Phillips, and R. S. Purves (2005), Simulation of snow shielding corrections for cosmogenic nuclide surface exposure studies, *Geomorphology*, *64*, 67–85.

Schildgen, T. F., D. Cosentino, B. Bookhagen, S. Niedermann, C. Yildirim, H. P. Echtler, H. Wittmann, and M. R. Strecker (2012), Multi-phased uplift of the southern margin of the Central Anatolian plateau, Turkey: A record of tectonic and upper mantle processes, *Earth Planet. Sci. Lett.*, *317-318*, 85–95, doi:10.1016/j.epsl.2011.12.003.

Schmidt, K., and D. R. Montgomery (1995), Limits to relief, *Science*, *270*, 617–620.

Schwanghart, W., and D. Scherler (2014), Short Communication: TopoToolbox 2 – MATLAB-based software for topographic analysis and modeling in Earth surface sciences, *Earth Surf. Dynam.*, *2*, 1–7, doi:10.5194/esurf-2-1-2014.

Seeber, L., and V. Gornitz (1983), River profiles along the Himalayan arc as indicators of active tectonics, *Tectonophysics*, *92*(4), 335–367.

Singh, A. K., B. Parkash, R. Mohindra, J. V. Thomas, and A. K. Singhvi (2001), Quaternary alluvial fan sedimentation in the Dehrandun Valley Piggyback Basin, NW Himalaya: Tectonic and palaeoclimatic implications, *Basin Res.*, *13*, 449–471.

Small, E. E., R. S. Anderson, and G. S. Hancock (1999), Estimates of the rate of regolith production using ^{10}Be and ^{26}Al from an alpine hillslope, *Geomorphology*, *27*, 131–150.

Snyder, N. P., K. X. Whipple, G. E. Tucker, and D. J. Merritts (2003), Importance of a stochastic distribution of floods and erosion thresholds in the bedrock river incision problem, *J. Geophys. Res.*, *108*(B2), 2117, doi:10.1029/2001JB001655.

Soille, P., J. Voigt, and R. Colombo (2003), Carving and adaptive drainage enforcement of grid digital elevation models, *Water Resour. Res.*, *39*, 1366, doi:10.1029/2002WR001879.

Srivastava, P., and G. Mitra (1994), Thrust geometries and deep structure of the outer and lesser Himalaya, Kumaon and Garhwal (India): Implications for evolution of the Himalayan fold-and-thrust belt, *Tectonics*, *13*, 89–109.

Srivastava, P., J. K. Tripathi, R. Islam, and M. K. Jaiswal (2008), Fashion and phases of late Pleistocene aggradation and incision in the Alaknanda River Valley, western Himalaya, India, *Quarter. Res.*, *70*, 68–80.

Stone, J. O. (2000), Air pressure and cosmogenic isotope production, *J. Geophys. Res.*, *105*, 23,753–23,759.

Styron, R. H., M. H. Taylor, and M. A. Murphy (2011), Oblique convergence, arc-parallel extension, and the role of strike-slip faulting in the High Himalaya, *Geosphere*, *7*, 582–596, doi:10.1130/GES00606.1.

Summerfield, M. A., and N. J. Hulton (1995), Natural controls of fluvial denudation rates in major world drainage basins, *J. Geophys. Res.*, *99*, 13,871–13,883.

Thakur, V. C., A. K. Pandey, and N. Suresh (2007), Late Quaternary–Holocene evolution of Dun structure and the Himalayan Frontal Fault zone of the Garhwal Sub-Himalaya, NW India, *J. Asian Earth Sci.*, *29*, 305–319, doi:10.1016/j.jseaes.2006.02.002.

Thiede, R. C., and T. A. Ehlers (2013), Large spatial and temporal variations in Himalayan denudation, *Earth Planet. Sci. Lett.*, *371-372*, 278–293.

Thiede, R., B. Bookhagen, J. R. Arrowsmith, E. Sobel, and M. Strecker (2004), Climatic control on rapid exhumation along the Southern Himalayan Front, *Earth Planet. Sci. Lett.*, *222*, 791–806, doi:10.1016/j.epsl.2004.03.015.

Thiede, R. C., T. A. Ehlers, B. Bookhagen, and M. R. Strecker (2009), Erosional variability along the northwest Himalaya, *J. Geophys. Res.*, *114*, F01015, doi:10.1029/2008JF001010.

Tripathy, G. R., and S. K. Singh (2010), Chemical erosion rates of river basins of the Ganga system in the Himalaya: Reanalysis based on inversion of dissolved major ions, Sr, and ^{87}Sr/^{86}Sr, *Geochem. Geophys. Geosyst.*, *11*, Q03013, doi:10.1029/2009GC002862.

Tucker, G. E. (2004), Drainage basin sensitivity to tectonic and climatic forcing: Implications of a stochastic model for the role of entrainment and erosion thresholds, *Earth Surf. Proc. Land.*, *29*, 185–205, doi:10.1002/esp.1020.

Tucker, G. E., and R. L. Bras (2000), A stochastic approach to modeling the role of rainfall variability in drainage basin evolution, *Water Resour. Res.*, *36*(7), 1953–1964, doi:10.1029/2000WR900065.

Vance, D., M. Bickle, S. Ivy-Ochs, and P. Kubik (2003), Erosion and exhumation in the Himalaya from cosmogenic isotope inventories of river sediments, *Earth Planet. Sci. Lett.*, *206*, 273–288, doi:10.1016/S0012-821X(02)01102-0.

Vannay, J. C., B. Grasemann, M. Rahn,W. Frank, A. Carter, and V. Baudraz (2004), Miocene to Holocene exhumation of metamorphic crustal wedges in the Himalayan orogen: Evidence for tectonic extrusion coupled to fluvial erosion, *Tectonics*, *23*, TC1014, doi:10.1029/2002TC001429.

von Blanckenburg, F. (2005), The control mechanisms of erosion and weathering at basin scale from cosmogenic nuclides in river sediment, *Earth Planet. Sci. Lett.*, *237*, 462–479.

von Blanckenburg, F., T. Hewawasam, and P. W. Kubik (2004), Cosmogenic nuclide evidence for low weathering and denudation in the wet, tropical highlands of Sri Lanka, *J. Geophys. Res.*, *109*, F03008, doi:10.1029/2003JF000049.

Webb, A. A. G., A. Yin, T. M. Harrison, J. Célérier, G. E. Gehrels, C. E. Manning, and M. Grove (2011a), Cenozoic tectonic history of the Himachal Himalaya (northwestern India) and its constraints on the formation mechanism of the Himalayan orogen, *Geosphere*, *7*(4), 1013–1061, doi:10.1130/GES00627.1.

Webb, A. A. G., A. K. Schmitt, D. He, and E. L. Weigand (2011b), Structural and geochronological evidence for the leading edge of the Greater Himalayan Crystalline complex in the central Nepal Himalaya, *Earth Planet. Sci. Lett.*, *304*, 483–495, doi:10.1016/j.epsl.2011.02.024.

Wesnousky, S. G., S. Kumar, R. Mohindra, and V. C. Thakur (1999), Uplift and convergence along the Himalayan Frontal Thrust of India, *Tectonics*, *18*(6), 967–976.

Whipple, K. X., and G. E. Tucker (1999), Dynamics of the stream-power river incision model: Implications for height limits of mountain ranges, landscape response timescales, and research needs, *J. Geophys. Res.*, *104*(B8), 17,661–17,674, doi:10.1029/1999JB900120.

Willett, S. D. (1999), Orogeny and orography: The effects of erosion on the structure of mountain belts, *J. Geophys. Res.*, *104*, 28,957–28,981.

Willett, S. D., and M. T. Brandon (2002), On steady states in mountain belts, *Geology*, *30*, 175–178.

Wittmann, H., F. von Blanckenbug, T. Kruesmann, K. P. Norton, and P. W. Kubik (2007), Relation between rock uplift and denudation from cosmogenic nuclides in river sediment in the Central Alps of Switzerland, *J. Geophys. Res.*, *112*, F04010, doi:10.1029/2006JF000729.

Wobus, C., A. M. Heimsath, K. X. Whipple, and K. V. Hodges (2005), Active out-of-sequence thrust faulting in the central Nepalese Himalaya, *Nature*, *434*, 1008–1011, doi:10.1038/nature03499.

Wobus, C., K. X. Whipple, E. Kirby, N. Snyder, J. Johnson, K. Spyropolou, B. Crosby, and D. Sheehan (2006), Tectonics from topography: Procedures, promise, and pitfalls, *Geol. Soc. Am. Spec. Pap.*, *398*, 55–74, doi:10.1130/2006.2398(04).

Wohl, E., and G. C. L. David (2008), Consistency of scaling relations among bedrock and alluvial channels, *J. Geophys. Res.*, *113*, F04013, doi:10.1029/2008JF000989.

Wulf, H., B. Bookhagen, and D. Scherler (2010), Seasonal precipitation gradients and their impact on fluvial sediment flux in the Northwest Himalaya, *Geomorphology*, *118*(1–2), 13–21, doi:10.1016/j.geomorph.2009.12.003.

Wulf, H., B. Bookhagen, and D. Scherler (2012), Climatic and geologic controls on suspended sediment flux in the Sutlej River Valley, western Himalaya, *Hydrol. Earth Syst. Sci.*, *16*, 2193–2217, doi:10.5194/hess-16-2193-2012.

Yanites, B. J., G. E. Tucker, and R. S. Anderson (2009), Numerical and analytical models of cosmogenic radionuclide dynamics in landslide-dominated drainage basins, *J. Geophys. Res.*, *114*, F01007, doi:10.1029/2008JF001088.

Yin, A. (2006), Cenozoic tectonic evolution of the Himalayan orogen as constrained by along-strike variation of structural geometry, exhumation history, and foreland sedimentation, *Earth Sci. Rev.*, *76*, 1–131.

Zeitler, P. K., et al. (2001), Crustal reworking at Nanga Parbat, Pakistan: Metamorphic consequences of thermal-mechanical coupling facilitated by erosion, *Tectonics*, *20*, 712–728, doi:10.1029/2000TC001243.